

AD-A064 660

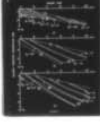
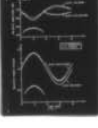
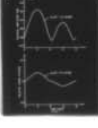
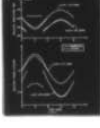
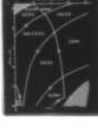
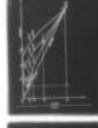
RENSSELAER POLYTECHNIC INST TROY N Y DEPT OF MATHEMA--ETC F/G 20/1
EFFECTS OF TIDALLY-VARYING SOUND SPEED ON ACOUSTIC PROPAGATION --ETC(U)
FEB 79 W L SIEGMANN, M J JACOBSON N00014-76-C-0288

UNCLASSIFIED

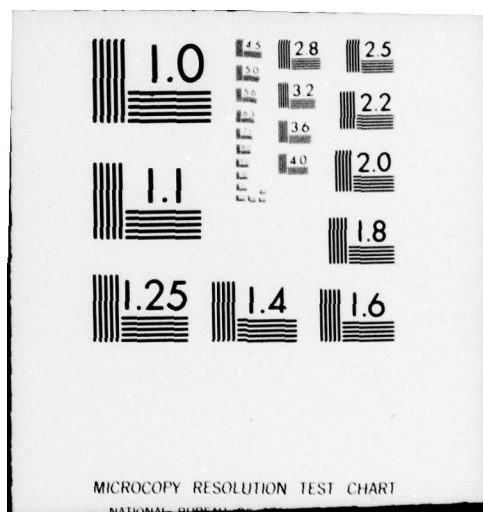
RPI-MATH-123

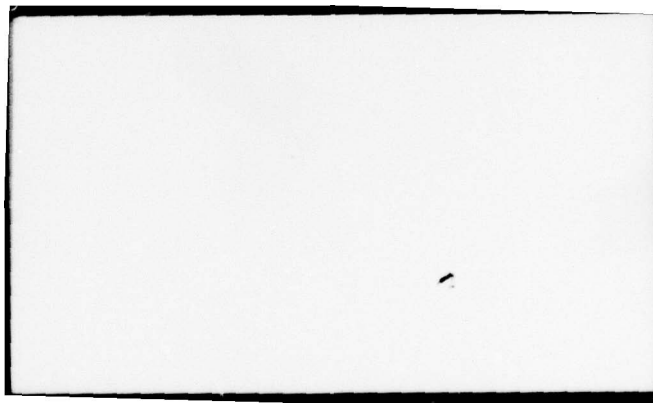
NL

1 OF 1
AD
A064660



END
DATE
FILMED
4-79
DDC





ACCESSION for	
NTIS	White Section <input checked="" type="checkbox"/>
DDC	Buff Section <input type="checkbox"/>
UNANNOUNCED	<input type="checkbox"/>
JUSTIFICATION	
BY	
DISTRIBUTION/AVAILABILITY CODES	
Dist.	AVAIL. and/or SPECIAL
A	

10

LEVEL II

6
Effects of Tidally-Varying Sound
Speed on Acoustic Propagation
over a Sloping Ocean Bottom

by

10
W. L./Siegmann, M. J./Jacobson,
K. G./Hamilton

9 Technical rept. 9

14

RPI-MATH-123

12 56 p.

Department of Mathematical Sciences

Rensselaer Polytechnic Institute

Troy, New York 12181

RPI Math. Rep. No. 123

February 1, 1979

11 1 Feb 79

This work was sponsored by

Code 222, Office of Naval Research

Contract No. N 00014-76-C-0288

NR 386-606

DDC
RECEIVED
FEB 15 1979
E

This document has been approved for public release and sale;
its distribution is unlimited.

408 898 79 02 09 010

ABSTRACT

The influence of sound-speed fluctuations on propagation of a CW signal in an ocean with a uniformly-sloping bottom and a horizontal surface is analyzed using ray theory. The mean sound-speed structure is modeled as bilinear, with bottomed source and receiver above and below the SOFAR axis, respectively. The horizontally-independent fluctuations oscillate with a 12-h period in the upper ocean. An examination is made of possible types of rays for down-slope propagation that might exist, depending on bottom-slope angle and source-receiver separation. The total acoustic field is investigated for its dependence on these parameters and time. For certain conditions when up to three rays comprise the mean total field, three patterns of time evolution are described, each of which may have significant amplitude variations. Numerically-computed examples of each type are presented. The linear relationships between phase variations of individual rays and the sound-speed fluctuations are derived. Then, formulas are developed to explain the most frequent behavior of the relative amplitude and phase of the multipath total field. Predictions from the formulas show very good agreement with the numerical calculations.

79 02 09 010

INTRODUCTION

This paper continues an investigation, begun in Ref. 1, into effects of certain combinations of ocean-environmental features on CW acoustic propagation. Reference 1 was concerned with the influence of a combination of spatially-uniform currents and upper-ocean, tidal sound-speed fluctuations on deep-ocean transmissions over a horizontal bottom. Under the model assumptions, it was found that total-field phase is affected by both current and sound-speed fluctuations, and that the latter more significantly contribute to amplitude variations. The small number of other acoustic studies in which combinations of oceanic variations have been considered are discussed in Ref. 1.

The primary purpose of this paper is to examine effects of sound-speed fluctuations on down-slope acoustic propagation over a nonhorizontal bottom. One model of interest is a uniformly-sloping bottom, which may be regarded as grossly approximating portions of the topography, at some locations, from continental or island shelves to the abyssal ocean. For simplicity we focus on this model, rather than possibly more generally-applicable ones consisting of several piecewise-linear segments. We note that our procedures permit extensions to such cases. Another reason for considering the uniform slope is that bottom variation has been excluded from most previous published propagation studies. Exceptions concern analyses of properties of refracted/bottom-reflected rays² and surface-reflected/bottom-reflected rays³ over a uniform slope. Another investigation⁴ showed how to analyze refracted/bottom-reflected rays propagating in an arbitrary direction over a uniform slope, by relating such

problems to ones in an ocean with a uniform horizontal sound-speed gradient. Environmental fluctuations were not considered in these studies. Moreover, their principal objective was relatively near-shore propagation, for which a linear or constant mean sound speed is appropriate. In the present case, for transmissions to depths below the SOFAR axis (at about 1000 m), a bilinear mean sound-speed profile is physically more reasonable, as well as analytically tractable (see, for example, Refs. 5, 6, and 7). In particular, we assume that both source and receiver are bottomed, above and below the SOFAR axis, respectively. In this paper we study acoustic propagation along a range normal to the constant-depth lines. This situation is a good approximation of some experimental conditions, is illustrative of sloping-bottom effects, and is relatively easy to analyze. Other propagation directions could be studied by applying and extending the procedures in Ref. 4. It is also assumed that for given bottom-slope angle α , the source-receiver distance R is short enough so the receiver depth does not exceed the abyssal ocean depth (about 4700 m). In order to understand the characteristics of the chosen model, we investigate intervals of values for α (between 7 and 15 degrees) and R (5 and 20 km), which include those typical of relatively short-range transmissions from off-shore sources.

In Sec. I the sound-speed fluctuations are modeled by pivoting sinusoidally, with semidiurnal period, the upper-ocean sound-speed gradient about the surface sound speed. The range R is assumed short enough to ignore horizontal variations. Motivation for this model in terms of the semidiurnal tide is

discussed in Ref. 1 and references therein. We remark that the model usefulness is not necessarily restricted to this particular form of fluctuations. In Sec. II the wide variety of possible types of RBR and SRBR rays that may occur are considered. It is found that the possibilities in the sloping-bottom geometry change dramatically, depending on values of parameters including α and R . Conditions are discussed so that the received total field consists of no more than three particular rays, and such cases are treated subsequently. Expressions are given for the amplitude and phase of these three rays at the receiver.

Numerical calculations for the relative phase and amplitude of the total field, as functions of time, are discussed in Sec. III. Three distinct patterns are found for the multipath cases, each of which may have significant amplitude variations. All show the interaction of the fluctuations and the sloping bottom, and for one type in particular, a consequence is the disappearance and later reappearance of a ray. In Sec. IV relations between the phase perturbations of individual rays and the sound-speed fluctuations are obtained. Then, formulas are derived for total-field variations in terms of ray-phase perturbations, for the most commonly-occurring type of behavior of the multipath total field. Comparisons between predictions from the formulas and computations in Sec. III show quite close agreement, in cases where conditions hold for validity of the formulas. Main results of the paper are summarized in Sec. V.

I. MODEL FORMULATION

We model a variable-depth, off-shore oceanic region by assuming that the ocean surface is flat and that the ocean bottom is a sloping plane intersecting the surface at an angle α . The line of intersection is regarded as the coast line of our model. We use a Cartesian coordinate system, with origin at some point on the coast. Increasing values of x and z indicate distance normal to the coast toward the deep ocean and oceanic depth, respectively, and the ocean surface is the plane $z = 0$. The y -direction is parallel to the coast so as to produce a right-handed coordinate system. The ocean bottom in this system is the plane $z = x \tan \alpha$. As discussed in the Introduction, we restrict attention in this paper to propagation normal to the coast, thereby eliminating dependence of both the range and the sound speed on the coordinate y . The sound source is placed on the ocean bottom, at depth d_o , and the receiver is also on the ocean bottom, at depth d_R . The horizontal distance between source and receiver is the range R and may be expressed as

$$R = (d_R - d_o) \cot \alpha . \quad (1)$$

Figure 1 illustrates the geometry of the propagation range and the parameters introduced above, along with some others to be discussed later. We note that our solution procedures could be adapted to analyze other hydrophone locations as well as propagation-range orientations. One additional constraint on our particular model is that the sloping bottom should not extend to a depth d_B of the abyssal ocean beyond the land-mass

rise, i.e. $d_R < d_B$. Otherwise, a piecewise-linear bottom model, in which the slope at depth d_B becomes parallel to the ocean surface, may be more appropriate.

We choose for our model of sound speed c the expression

$$c(x, z, t) = c_S[1+f(z)] + \tilde{c}(x, z, t), \quad (2)$$

where c_S is the fixed sound speed at the ocean surface above the source, i.e. at $x = d_0 \cot \alpha$, and t is time. The function $f(z)$ describes the depth variation of sound speed in the absence of \tilde{c} , which incorporates changes due, for example, to tidal effects. The dimensionless quantities f and $\tilde{c} c_S^{-1}$ satisfy $\tilde{c} c_S^{-1} \ll f \ll 1$.

We specify the form of the mean variation $f(z)$ as a bilinear model, of a type used previously (for a recent example, see Ref. 1), to reasonably approximate measured deep-ocean profiles while simplifying the acoustical analysis. We thus select

$$f(z) = -zg_1 c_S^{-1}, \quad 0 \leq z \leq d_A \quad (3a)$$

and

$$f(z) = [c_A - c_S + g_2(z-d_A)]c_S^{-1}, \quad d_A \leq z \leq x \tan \alpha. \quad (3b)$$

In Eqs. (3), c_A is the value of the mean sound speed which occurs at the SOFAR axis depth d_A . The quantities g_1 and g_2 are the magnitudes of the sound-speed gradients above and below the SOFAR axis, respectively. We may now express the mean sound speed at the sound source c_0 and at the receiver c_R as

$$c_o = c_s - g_1 d_o \quad (4a)$$

and

$$c_R = c_A + g_2 (d_R - d_A) , \quad (4b)$$

where we have chosen to consider the case $d_o < d_A < d_R$ exclusively in this paper.

Typical parameter values appropriate for studying sound propagation initiated near Bahaman shores of the Sargasso Sea⁸ are $c_s = 1541 \text{ m sec}^{-1}$, $c_A = 1487 \text{ m sec}^{-1}$, and $d_A = 1000 \text{ m}$, leading to the value 0.0540 for g_1 , and $g_2 = 0.0146$. For definiteness, we will use these fixed numerical values in computations throughout this paper. Nonetheless, we seek to construct a model with more generality and wider possible application than just to this oceanic region or to any specific acoustic-propagation range. Thus, we will present results for source-receiver distances R between 5 and 20 km, and for bottom-slope angles α in the range between 7 and 15 degrees. These values include those typical of relatively short-range transmissions from off-shore sources. In this paper we will only discuss investigations for a fixed source depth $d_o = 300 \text{ m}$. Results for this case were regarded as typical of source depths not near either the surface or SOFAR axis. For this fixed value of d_o and given α and R values, it follows that d_R is determined by Eq. (1). For a value of $d_B = 4700 \text{ m}$, requiring the receiver remain on the slope and below the SOFAR axis imposes

$$700 \text{ m} < R \tan \alpha < 4400 \text{ m} . \quad (5)$$

We note that other fixed parameter values and intervals of R and α values can be examined by further application of our solution procedures.

We consider next the effect of tidal variations on sound speed via \tilde{c} . An earlier study¹ considered the tidal effects on sound speed in the deep ocean, using observations of temperature fluctuations (as in Ref. 9), an analysis of state equations to relate sound-speed fluctuations to those of temperature, and the assumption of sufficiently short propagation ranges. The deep-ocean model in Ref. 1 includes an oscillation with period 12 h of both the depth $\hat{d}_A(t)$ of minimum sound speed and the gradient above $\hat{d}_A(t)$, with the surface sound speed remaining fixed. The semidiurnal component is a strong feature of temperature fluctuations nearer to shore as well, and frequency spectra of currents there indicate even more concentration of energy in this component.¹⁰ Since we are aware of no evidence to invalidate the deep-ocean model for \tilde{c} in the continental-slope regions, we shall employ it here. We note that in any application of our model, more general time variation could be incorporated if observations warranted. Moreover, certain other forms of vertical structures, either singly or in combination, could be treated by the method in Sec. IV.

Therefore, we set

$$\tilde{c}(z,t) = \begin{cases} \mu z \sin(\pi t/6) & , \quad 0 \leq z \leq \hat{d}_A(t) \\ 0 & , \quad z > \hat{d}_A(t) \end{cases} \quad (6)$$

where μ is the magnitude of the perturbation gradient, measured in sec^{-1} , and t is measured in hours so that for convenience the

tidal perturbation at $t = 0$ is absent. The time-dependent SOFAR axis depth is closely approximated by¹

$$\hat{d}_A(t) = d_A [1 + \mu(g_1 + g_2)^{-1} \sin(\pi t/6)] . \quad (7a)$$

It follows that the time-dependent sound speed $\hat{c}_A(t)$ at $\hat{d}_A(t)$ is

$$\hat{c}_A(t) = c(\hat{d}_A(t), t) = c_A + \Delta \sin(\pi t/6) , \quad (7b)$$

where the non-negative parameter

$$\Delta = \mu d_A g_2 (g_1 + g_2)^{-1} \quad (7c)$$

is the amplitude of the sound-speed fluctuation of $\hat{d}_A(t)$. Values of Δ up to 0.30 m sec^{-1} will be examined here, as in Ref. 1.

Equations (6) and (7) imply that the maximum variation of sound speed with time occurs at the mean SOFAR depth d_A and is equal to $\Delta g_2^{-1} (g_1 + g_2)$. Figure 2 illustrates the model by showing representative sound-speed structures corresponding to maximum, zero, and minimum perturbations.

II. RAY ANALYSIS

We assume that acoustic propagation occurs under conditions for which ray theory is valid. In this section, we discuss the ray geometry and amplitude and phase of any ray in the variable-depth channel of Sec. I with no sound-speed perturbations. Thus, the sound speed is given by Eq. (2) with $\tilde{c} = 0$ and Eq. (3), and parameter values are as in Sec. I. It follows that rays consist of piecewise circular arcs. Moreover, because the vertical plane containing the source-receiver direction is perpendicular to the

coast line of our model, rays remain entirely in this plane; otherwise, rays making bottom reflections would be deflected out of this plane.⁴ If θ is the inclination angle of a ray measured positive clockwise from the horizontal, then the usual form of Snell's law,

$$c^{-1} \cos \theta = \text{constant}, \quad (8)$$

is valid, although the constant changes after each bottom reflection.

We now consider determination of the rays. In order to obtain analytical ray descriptions which are also numerically accurate, we begin by hypothesizing a possible ray path. For our model, rays can be characterized by specifying a pair of integers $[K, L]$, where K and L are the number of surface and bottom reflections, respectively. We note that under our particular model assumptions, it can be shown by geometrical considerations and numerical calculations that there exists at most one ray for each pair of integers $[K, L]$. Next, the equations governing the ray are determined, which in general form a nonlinear system for the ray angle at the source, θ_o , and other parameters. Numerical root-finding procedures are then used to determine values for the variables. The validity of each solution is established by testing that the ray does not pass outside the ocean on its way to the receiver.

The simplest conceivable ray has $K = L = 0$. Its governing equations are Eqs. (1), (4), (8), and

$$R = g_1^{-1}(c_A \tan \theta_A - c_o \tan \theta_o) + g_2^{-1}(c_A \tan \theta_A - c_R \tan \theta_R), \quad (9a)$$

where θ_A and θ_R are (positive) ray angles at the SOFAR axis and receiver, respectively. Equation (9a) is derived in, for example, Ref. 4. The $[0,0]$ ray is illustrated in Fig. 1. The angles θ_O , θ_A , and θ_R are shown and are all positive. The requirement that this ray never reaches the surface may be expressed as

$$\theta_O > -\cos^{-1}(c_O c_S^{-1}) . \quad (9b)$$

Additional inequalities which are imposed for given α and R are Eq. (5) and

$$\theta_R \geq \alpha , \quad (10)$$

which precludes acoustic energy from reaching the receiver through the ocean bottom.

Numerical results for the existence of the $[0,0]$ ray are shown in Fig. 3. Values for θ_O may be found by iterating for $\tan \theta$ using Newton's method for most (α, R) pairs in the Figure. Equation (10) is satisfied only above and to the left of the curve labeled 3 in Fig. 3. Moreover, Eq. (9b) is violated below curve 8. Since the first inequality of Eq. (5) is not satisfied in the shaded area above curve 1, it follows that the $[0,0]$ ray exists only in the region of Fig. 3 bounded by curves 1, 3, and 8. We remark here that the second inequality of Eq. (5) fails in the other shaded area, below curve 7.

Another ray of interest has $K = 1$ and $L = 0$, and is also illustrated in Fig. 1. The equations⁵ determining the geometry of the $[1,0]$ ray are Eqs. (1), (4), (8), (10),

$$R = g_1^{-1} (c_A \tan \theta_A - c_O \tan \theta_O - 2c_S \tan \theta_S) \\ + g_2^{-1} (c_A \tan \theta_A - c_R \tan \theta_R) , \quad (11a)$$

and

$$\theta_O < -\cos^{-1}(c_O c_S^{-1}) , \quad (11b)$$

where θ_S is the (positive) ray angle at the surface. As illustrated in Fig. 3, the $[1,0]$ ray is found by numerical calculations to exist in the region of the (α, R) plane bounded by the curves labeled 2, 4, and 8. Below curve 4, the $[1,0]$ ray fails to exist because Eq. (10) is violated, while below curve 8, the $[1,0]$ ray disappears because Eq. (11b) is violated.

The third type of ray of principal interest in this paper is that with $K = 2$ and $L = 1$. As illustrated in Fig. 1, its bottom reflection is at depth d_{B1} , where the bottom incident ray angle is θ_{B1} and the sound speed c_{B1} is, from Eqs. (2) and (3a),

$$c_{B1} = c_S - g_1 d_{B1} . \quad (12a)$$

Additional conditions needed to specify the $[2,1]$ ray are Eqs. (1), (4), (8), (10),

$$R = g_1^{-1} \{ c_A \tan \theta_A - 2c_S (\tan \theta_{S1} + \tan \theta_{S2}) - c_O \tan \theta_O \\ + c_{B1} [\tan \theta_{B1} - \tan(2\alpha - \theta_{B1})] \} + g_2^{-1} (c_A \tan \theta_A - c_R \tan \theta_R) , \quad (12b)$$

$$(d_{B1} - d_O) \cot \alpha = g_1^{-1} (c_{B1} \tan \theta_{B1} - 2c_S \tan \theta_{S1} - c_O \tan \theta_O) , \quad (12c)$$

and

$$2\alpha - \theta_{B1} < -\cos^{-1}(c_{B1} c_S^{-1}) . \quad (12d)$$

The angles θ_{S1} and θ_{S2} are the (positive) ray angles at the first and second surface reflections, as shown in Fig. 1. Note that Snell's law provides two independent equations, since the bottom reflection changes the constant in Eq. (8).

The numerical calculations for the [2,1] ray were performed by first estimating $\tan \theta_{B1}$ and c_{B1} . Then, Snell's law was used to determine θ_0 and θ_{S1} , after which Newton's method was applied to Eqs. (12a) and (12c) to converge to the correct value for c_{B1} for the estimated value of $\tan \theta_{B1}$. Values were obtained for θ_{S2} , θ_A , and θ_R from Snell's law, and $\tan \theta_{B1}$ was re-estimated from Eq. (12b). This process was continued until convergence was obtained. Efficient calculations for this ray, as well as for others, relied on accurate initial estimates. It was found that the [2,1] ray exists over most of the (α, R) plane in Fig. 3, although not below curve 5 because Eq. (10) is violated. In addition, we assumed that the source hydrophone is directional, transmitting significant sound energy only for launch angles θ_0 satisfying $|\theta_0|$ less than some value θ_{OD} . This can be accomplished, for example, by using an omnidirectional "point" source with a reflector, as described for example in Ref. 11, or an array of omnidirectional sources. With the value $\theta_{OD} = 40^\circ$, the [2,1] ray is restricted to the left of curve 6 in Fig. 3.

For certain parameter values considered here, rays of type [0,L] exist, with $L \geq 1$ bottom reflections which must lie above the SOFAR axis. As indicated in Fig. 3, we have shown that various members of this family of rays occur for the shallow receiver positions above curve 2. When these rays exist, they could in principle be significant contributors to the total received

field, since they suffer relatively small spreading and bottom loss because of their short path length and near-grazing bottom incident angles. On the other hand, for the latter reason, such rays are particularly sensitive to actual nonlinear bottom topography in any specific experiment. For our investigations of total field in later sections, we choose parameter values for which rays of this type do not occur.

We remark that the combination of bilinear sound speed and sloping bottom in our model permits a remarkably rich variety of rays. Figure 3 suggests the patterns that can arise, but depending on assumptions and parameter values, the situation can become more complicated. For instance, if θ_{OD} is larger than 40° , not only does the [2,1] ray exist over more of the (α, R) plane shown, but also new rays may occur. The [3,2] ray may be present, since its initial angle ranges from $\theta_o = -40.5^\circ$ for $(\alpha, R) = (7^\circ, 17 \text{ km})$ to $\theta_o = -85.0^\circ$ for $(\alpha, R) = (15^\circ, 5 \text{ km})$, for the (α, R) values in Fig. 3. Indeed, other rays with more than two surface reflections could also occur. The importance of these steep rays to the total field would depend critically on such factors as bottom loss and scattering. As another example, a piecewise-linear bottom dramatically changes the ray possibilities; more than one ray sometimes occur for given numbers $[K, L]$ of surface and bottom reflections.

In view of the foregoing considerations, for subsequent analysis of the total received field, we shall restrict (α, R) values to the regions in Fig. 3 where some or all of the [0,0], [1,0], and [2,1] rays, but no others, exist. We henceforth denote

these as the $n = 1, 2$, and 3 rays, respectively. Note that for the rays considered in this paper, we can identify n with $K + 1$.

The travel times T_n for rays $n = 1$ and $n = 2$ can be adapted from Ref. 5, while that for ray $n = 3$ can be calculated using procedures of Ref. 5. The results are

$$T_1 = g_1^{-1} \ln[c_O(1+\sin\theta_A)c_A^{-1}(1+\sin\theta_O)^{-1}] + g_2^{-1} \ln[c_R(1+\sin\theta_A)c_A^{-1}(1+\sin\theta_R)^{-1}] , \quad (13a)$$

$$T_2 = g_1^{-1} \ln[c_O(1-\sin\theta_S)(1+\sin\theta_A)c_A^{-1}(1+\sin\theta_O)^{-1} \times (1+\sin\theta_S)^{-1}] + g_2^{-1} \ln[c_R(1+\sin\theta_A)c_A^{-1}(1+\sin\theta_R)^{-1}] , \quad (13b)$$

and

$$T_3 = g_1^{-1} \ln\{c_O(1-\sin\theta_{S1})(1+\sin\theta_{B1})(1-\sin\theta_{S2})(1+\sin\theta_A) \times c_A^{-1}(1+\sin\theta_O)^{-1}(1+\sin\theta_{S1})^{-1}(1+\sin\theta_{S2})^{-1}[1+\sin(2\alpha-\theta_{B1})]^{-1}\} + g_2^{-1} \ln[c_R(1+\sin\theta_A)c_A^{-1}(1+\sin\theta_R)^{-1}] . \quad (13c)$$

These expressions can be evaluated, using Eqs. (1), (4), (8), (12a), and (12c) where appropriate, once the source angles θ_O of the three rays have been determined numerically.

The formulas for the geometrical spreading loss can be developed from results and methods in Ref. 2:

$$\Lambda_1 = Rc_O^2 \sin\theta_R \sec^3\theta_O |\tan\theta_O [g_1^{-1}(c_A^{-1}\cot\theta_A - c_O^{-1}\cot\theta_O) + g_2^{-1}(c_A^{-1}\cot\theta_A - c_R^{-1}\cot\theta_R)]| , \quad (14a)$$

$$\Lambda_2 = R c_o^2 \sin \theta_R \sec^3 \theta_o \tan \theta_o [g_1^{-1} (c_A^{-1} \cot \theta_A - 2c_S^{-1} \cot \theta_S - c_o^{-1} \cot \theta_o) + g_2^{-1} (c_A^{-1} \cot \theta_A - c_R^{-1} \cot \theta_R)] , \quad (14b)$$

and

$$\begin{aligned} \Lambda_3 = R \sin \theta_R \sec \theta_o & \left(g_1^{-1} \{ c_{B1}^2 \sec^2 \theta_{B1} \tan \theta_o (c_{B1}^{-1} \cot \theta_{B1} - c_o^{-1} \cot \theta_o - 2c_S^{-1} \cot \theta_S) \right. \\ & + [\cot(2\alpha - \theta_{B1}) - \cot \theta_{B1}] (dc_{B1}/d\theta_o) \} \\ & + c_{B1} \sec^2(2\alpha - \theta_{B1}) [(1 + \tan(2\alpha - \theta_{B1}) \cot \theta_{B1}) (dc_{B1}/d\theta_o) \\ & - c_{B1} \tan \theta_o \tan(2\alpha - \theta_{B1}) \cot \theta_{B1}] \left\{ g_1^{-1} [c_A^{-1} \cot \theta_A - 2c_S^{-1} \cot \theta_S - c_{B1}^{-1} \cot(2\alpha - \theta_{B1})] \right. \\ & \left. \left. + g_2^{-1} (c_A^{-1} \cot \theta_A - c_R^{-1} \cot \theta_R) \right\} \right) [R_{B1} R^{-1} + (1 - R_{B1} R^{-1}) \cos \theta_{B1} \sec(\theta_{B1} - 2\alpha)] . \quad (14c) \end{aligned}$$

In Eq. (14c) the derivative term is

$$dc_{B1}/d\theta_o = c_o \tan \theta_o \sec \theta_o (csc \theta_{B1} - csc \theta_o - 2csc \theta_{S1}) (\cot \theta_{B1} - \cot \alpha)^{-1} , \quad (14d)$$

and the horizontal distance between source and bottom reflection is

$$R_{B1} = g_1^{-1} (c_o - c_{B1}) \cot \alpha . \quad (14e)$$

We assume the sound source emits a harmonic signal with circular frequency ω and with maximum amplitude unity, i.e. 1 dyn cm^{-2} at distance 1 m. It follows that ray n arrives at the receiver in the form $A_n \sin(\omega t - \phi_n)$. The amplitude A_n is affected by source directivity and by the physical processes of spreading loss, boundary loss, attenuation, and scattering, but the latter two effects are excluded here. At any surface

reflection, the model of Mackenzie¹² leads to no amplitude loss and a phase shift of π . The loss B_3 and phase shift ϕ_3 at the bottom reflection of ray 3 may also be computed from formulas in Ref. 12. Two parameters characterizing bottom properties appear in the formulas for B_3 and ϕ_3 . The first (called α/β in Ref. 12) is the ratio of complex to real parts of the bottom attenuation factor. Although this quantity in general depends on acoustic frequency and bottom composition, a frequency-independent value may be derived,¹² and we choose a value of 0.0158 for a bottom which has been used for the Sargasso Sea area.¹³ The second parameter, σ , is the impedance ratio of the bottom,

$$\sigma = (\rho_x c_x) (\rho_{B1} c_{B1})^{-1}, \quad (15a)$$

where the corresponding bottom density ρ_x and sound speed c_x are $\rho_x = 2.00 \text{ gm cm}^{-3}$ and $c_x = 1757 \text{ m sec}^{-1}$. An approximate formula for water density ρ_{B1} (in gm cm^{-3}) at depth d_{B1} (in m), which can be derived from Eq. (20) of Ref. 14, is

$$\rho_{B1} = 1.0243 + (8.2716 \times 10^{-6}) d_{B1}. \quad (15b)$$

Thus, the amplitude of ray n can be written as

$$A_n = \Lambda_n^{-1/2} B_n D(\theta_o), \quad (16a)$$

if we define $B_1 = B_2 = 1$. The directivity factor D is normalized to a maximum value of 1. We note that our definition of θ_{oD} requires $D(\theta_o)$ to be significantly less than 1 for $|\theta_o| > \theta_{oD}$. Similarly if $\phi_1 = \phi_2 = 0$, the phases ϕ_n satisfy

$$\phi_n = \omega T_n - (n-1)\pi - \phi_n . \quad (16b)$$

Using Eqs. (13) and (14), the values for the functions in Eq. (16) are found after the numerically-determined quantities such as θ_0 are known.

III. TOTAL-FIELD RESULTS

Under the conditions described in Sec. II for which Fig. 3 is applicable, the total field at the receiver is given by

$$A \sin(\omega t - \phi) = \sum_{n=1}^3 A_n \sin(\omega t - \phi_n) , \quad (17a)$$

in which the amplitude A and phase ϕ are determined from

$$S = \sum_{n=1}^3 A_n \sin \phi_n , \quad C = \sum_{n=1}^3 A_n \cos \phi_n , \quad (17b)$$

and

$$A = (S^2 + C^2)^{1/2} , \quad \sin \phi = S/A , \quad \cos \phi = C/A . \quad (17c)$$

Expressions for A_n and ϕ_n are given in Eqs. (16). The amplitude A_n is set to zero if ray n is absent.

The preceding section focused on ray analysis in the absence of the sound-speed perturbation \tilde{c} . Here, we present results of the numerical investigation of Eqs. (17) for our model including \tilde{c} . Under the assumptions in Sec. I, the time variation of the sound speed is sufficiently slow that it can be ignored during the time required for an acoustic signal to propagate from source to receiver. From Eq. (6) it follows that rays in the perturbed medium are of the same form as those when $\tilde{c} = 0$. Moreover, the

launch angle θ_0 and other variables for a ray of type $n = 1, 2$, or 3 can be calculated from the appropriate governing equations in Sec. II, but with perturbed values of g_1 , d_A , and c_A . Given values of α and R , the diagram for existence of rays in the perturbed medium differs only slightly from Fig. 3, specifically in the location of certain boundary curves. A number of different combinations of values for parameters α and R were selected, but all the calculations we shall discuss here used $\Delta = 0.3 \text{ m sec}^{-1}$, $\omega = 206 \text{ Hz}$, and $D(\theta_0) = 1$ for $|\theta_0| \leq 40^\circ$ and 0 for larger $|\theta_0|$. Results for this Δ are presumably typical of those for other (small) values of Δ . The directivity pattern used here may be regarded as an idealization of more realistic patterns (for examples constructed from endfire linear arrays of isotropic point sources, see Ref. 15). Time was varied over 12 h since that interval is the period of \tilde{c} .

From the many cases examined, several characteristic types of behavior in the total field were observed, which we now discuss. The simplest type is obviously when α and R are such that only a single ray appears, which from Fig. 3 would be either the $n = 2$ or 3 ray. Typically, amplitude A varies only slightly with time; the maximum variation of relative amplitude over 12 h was found to be less than 1 dB in all single-path cases examined. Phase ϕ is sinusoidal in time, with period 12 h. The peak-to-peak phase variation was 0.42 cycles for the $n = 2$ ray when $(\alpha, R) = (15^\circ, 7 \text{ km})$. It would be anticipated that single-path cases possess a simple relationship between environmental and acoustical variations. This is, of course, an important consideration in certain acoustical

experiments which monitor ocean processes. In our model, it is significant that single-path cases occur at relatively longer ranges than multipath, as is clear from Fig. 3.

As shown in Fig. 3, other values of α and R permit two rays, specifically the pairs $(n=0, n=1)$ and $(n=1, n=2)$. Total-field amplitude and phase are illustrated, for an example of the former case, with $(\alpha, R) = (11^\circ, 7 \text{ km})$, in the solid curves of Fig. 4. The amplitude, which is relative to that of the unit-amplitude source, is a smooth, roughly sinusoidal function of time, with peak-to-peak variation of 9.8 dB. We note that individual ray amplitudes have very small amplitude variation with time, analogous to the single-path case. Hence, the conclusion follows that the solid amplitude curve in Fig. 4 reflects multipath effects. The phase, shown relative to 1.0 cycles for clarity, is also smooth, is virtually sinusoidal, and has peak-to-peak variation of 0.68 cycles. This pattern was the most common one among our double-path results, and we shall refer to it as type I behavior of the multipath total field. A theoretical description of this case will be discussed in Section IV.

Another variety of double-path behavior is shown by the solid curves for $(\alpha, R) = (12^\circ, 8 \text{ km})$ in Fig. 4, which we denote by type II. The mean state possesses $n = 0$ and 1 rays, but the $n = 0$ ray is nearly tangential to the bottom at the receiver. The sound-speed perturbation can cause the ray to violate Eq. (10), thereby removing the ray from the total field. This occurs in Fig. 4 from about $t = 1.2 \text{ h}$ to 4.8 h , during which period the phase and amplitude display the characteristics of single-path propagation

discussed earlier. Outside this time interval, the double-path behavior is typical of type I. The jump in amplitude at the transition points is about 9.5 dB. In combination with the approximately 7.5 dB variation in amplitude from $t = 4.8$ h to $t = 9$ h, it is clear that substantial amplitude variation will occur in this example. The phase, shown relative to 0.75, is discontinuous at the exit and entrance points of the $n = 0$ ray. We note that the actual phase jumps at those points are the differences shown on Fig. 4 (about ± 0.4 cycles) modulo one cycle. Type II behavior points out another effect of the interaction of sound-speed fluctuations and the sloping bottom.

An example of a third class of double-path behavior found among our computational results is illustrated in Fig. 5. This is an $n = 2$ and 3 case for $(\alpha, R) = (11^\circ, 15 \text{ km})$, with peak-to-peak amplitude and phase variations of 7.1 dB and 0.31 cycles, respectively. However, neither relative amplitude nor relative phase of this type III case is close to the sinusoidal curves typical in type I. For example, amplitude fades occur near $t = 6$ h and 12 h, over time scales much shorter than the scale of environmental variation. This pattern has been observed in many multipath studies (see for example Refs. 1 and 16), although typically in situations with more rays than are present here. In the mean state, the phases of the $n = 2$ and 3 rays are nearly π radians apart, and the total-field amplitude is only about 20% of the individual amplitudes. Thus, with the perturbation applied, both amplitude and phase are sensitive to small differences in the rates of perturbation of the phases of the individual arrivals.

This sensitivity precludes application of the theoretical analysis to be discussed in Sec. IV.

From Fig. 3 it is seen that for certain (α, R) combinations, all three rays can contribute to the total field. Exactly as for the double-path calculations, type I behavior was most frequently found for triple-path calculations. Relative phase and amplitude for a typical case, $(\alpha, R) = (8^\circ, 8 \text{ km})$ shown as solid curves in Fig. 6, are very similar to the analogous curves in Fig. 4. The amplitude curve shows a total variation of 7.8 dB and is somewhat less symmetric about $t = 6 \text{ h}$ than the corresponding curve in Fig. 4. Peak-to-peak phase variation is 0.77 cycles.

Type II behavior also occurs for triple-path cases. Figure 3 shows that either the $n = 1$ or $n = 3$ rays can be lost near boundary curves 3 and 6, respectively. We shall not discuss cases near boundary 8, where two rays can disappear. Phase and amplitude are shown in Fig. 6 for $(\alpha, R) = (10^\circ, 10.5 \text{ km})$, for which the $n = 1$ ray is absent between $t = 0.5 \text{ h}$ and $t = 5.5 \text{ h}$. In that interval, the double-path behavior is characteristic of type I. In fact, over each continuous portion of the curves, typical type I behavior occurs. We remark that although type III double-path behavior is conceivable when one ray is lost from a triple-path case, we never observed this situation. From Fig. 6, the total-field amplitude variation is about 12.2 dB, while the changes over each continuous portion in this example are about 2 dB. The phase, shown in Fig. 6 relative to 1.1 cycles for clarity, is approximately sinusoidal over its continuous portions. As in Fig. 4, the actual phase jumps could be larger than

suggested by Fig. 6, in which phase modulo one cycle is shown. We note finally that type III triple-path behavior could conceivably occur for three rays if, for example, the phase of the vector sum of the $n = 2$ and 3 rays happened to differ by nearly π radians from the phase of the (strongest) $n = 1$ ray. However, this was not observed among the triple-path cases we examined.

IV. APPROXIMATE TOTAL-FIELD MODEL

The computational results of Sec. III suggest that analytical approximation of the total field phase and amplitude should be possible for behavior of type I (and for continuous portions of type II cases). The first step is to approximately determine perturbations to phases of individual ray arrivals produced by the sound-speed perturbation. Then, we shall show how these results are useful in approximating the total field.

From Eqs. (7), the time-dependent SOFAR-axis depth $\hat{d}_A(t)$ can be expressed in terms of $\hat{c}_A(t)$, and similarly for the time-dependent upper-layer gradient. Thus, the time dependence of the phase ϕ_n of any ray ($n = 1, 2$, or 3) can be considered a consequence of the time dependence of the single environmental quantity $\hat{c}_A(t)$. Define $\Delta\phi_n$ as the phase fluctuation of ray n due to the sound-speed perturbation. From the first two terms of a Taylor series expansion and Eq. (7b), it follows that

$$\Delta\phi_n(t) \equiv \phi_n(\hat{c}_A) - \phi_n(c_A) \doteq (\partial\phi_n/\partial c_A) \Big|_{c_A=c_A} \hat{\Delta}(t), \quad (18a)$$

where

$$\hat{\Delta}(t) \equiv \hat{c}_A(t) - c_A = \Delta \sin(\pi t/6) . \quad (18b)$$

Partial differentiation is used in Eq. (18a) to indicate that $\Delta\phi_n$ depends on other variables; just one term appears in Eq. (18a) because \hat{c}_A is regarded as the only time-dependent environmental parameter. Next, we use Eq. (16b) to write

$$\left(\partial\phi_n / \partial\hat{c}_A \right) \Big|_{c_A} = \omega \left(\partial T_n / \partial\hat{c}_A \right) \Big|_{c_A} \equiv \beta_n , \quad (18c)$$

which is exact for $n = 1$ and 2 but ignores the contribution $-(\partial\phi_3 / \partial\hat{c}_A) \Big|_{c_A}$ for $n = 3$. This term can be estimated, with difficulty, from Eqs. (15) and the equations for the $n = 3$ ray. Alternatively, its effects can be shown to be negligible by actual numerical calculations for the perturbed $n = 3$ ray (for illustration, a typical value of $|(\partial\phi_3 / \partial\hat{c}_A) \Big|_{c_A} \Delta|$ is .001 cycles for our parameter values and $(\alpha, R) = (10^\circ, 15 \text{ km})$). Once an expression for the travel time derivative is obtained, $\Delta\phi_n$ is approximated through Eqs. (18).

Direct calculation of $\partial T_n / \partial\hat{c}_A$ from Eqs. (13) is feasible but very unwieldy, because of the implicit relationships among \hat{c}_A and the variables describing the ray geometry. By differentiating Eqs. (13) and using Eqs. (2), (3), (7c), (8), (9a), (11a), (12b), (12c), and (12d), it can be shown after considerable manipulation that Eqs. (18) yield:

$$\begin{aligned} \Delta\phi_1(t) = & \omega \mu g_1^{-2} \sin(\pi t/6) \{ \ln [c_O(1+\sin\theta_A)c_A^{-1}(1+\sin\theta_O)^{-1}] \\ & - c_s(c_A^{-1} \sin\theta_A - c_O^{-1} \sin\theta_O) \} , \end{aligned} \quad (19a)$$

$$\begin{aligned} \Delta\phi_2(t) = & \omega\mu g_1^{-2} \sin(\pi t/6) \{ \ln [c_O(1-\sin\theta_S)(1+\sin\theta_A)c_A^{-1} \\ & \times (1+\sin\theta_O)^{-1}(1+\sin\theta_S)^{-1}] - c_S(c_A^{-1}\sin\theta_A - 2c_S^{-1}\sin\theta_S \\ & - c_O^{-1}\sin\theta_O) \} , \end{aligned} \quad (19b)$$

and

$$\begin{aligned} \Delta\phi_3(t) = & \omega\mu g_1^{-2} \sin(\pi t/6) \{ \ln [c_O(1-\sin\theta_{S1})(1+\sin\theta_{B1}) \\ & \times (1-\sin\theta_{S2})(1+\sin\theta_A)c_A^{-1}(1+\sin\theta_O)^{-1}(1+\sin\theta_{S1})^{-1} \\ & \times (1+\sin\theta_{S2})^{-1}[1+\sin(2\alpha-\theta_{B1})]^{-1}] - c_S[c_A^{-1}\sin\theta_A \\ & - 2c_S^{-1}\sin\theta_{S1} - 2c_S^{-1}\sin\theta_{S2} + c_{B1}^{-1}\sin\theta_{B1} - c_{B1}^{-1}\sin(2\alpha-\theta_{B1}) \\ & - c_O^{-1}\sin\theta_O] \} . \end{aligned} \quad (19c)$$

Equations (19) can be evaluated from previously-computed geometric quantities of the unperturbed rays.

We note that the phase perturbations are independent of g_2 and θ_R , parameters characterizing the ray geometry below the SOFAR axis. That is, the sound-speed fluctuation produces changes in ray geometry below the SOFAR axis, but these changes do not affect the phase perturbations in Eqs. (19). To the order of terms retained in Eqs. (19), phase perturbations depend only on those portions of the rays above the SOFAR axis.

One way to present the results of Eqs. (19) is to regard $\Delta\phi_n(t)$ as a function of α and R and show the level curves of this function. In view of Eqs. (18), it is sufficient to consider level curves of β_n . Given values of α and R , the quantity β_n

could be obtained by interpolation from the level curves. It is particularly convenient to plot the level curves for $n=1$ and 2 with respect to R and $R \tan \alpha = d_R - d_O$ (by Eq. (1)). To see this, we note that for any ray, β_n depends only on the mean ray geometry above the SOFAR axis. Consequently, β_n will be the same for all members of each family of rays with identical ray lobes for $z < d_A$. Since the $n = 1$ and 2 rays in particular are unaffected by the ocean bottom for $z < d_A$, members of any such family correspond to rays reaching a receiver at depth d_R related to R and α by Eq. (1). Because the locus of receiver depths is a circular arc, the level curves themselves are circular arcs in the $(d_R - d_O, R)$ plane. Using values for quantities previously determined numerically, we plot level curves for β_1 and β_2 in this plane as solid curves in Fig. 7(a) and 7(b), respectively. Also indicated by dashes are curves 1 and 2, of minimum ($\alpha = 7^\circ$) and maximum ($\alpha = 15^\circ$) bottom angles, respectively. In addition, the curves 3 and 4, demarcating the existence of the $n=1$ and 2 rays as described in connection with Fig. 3, are shown in Figs. 7(a) and 7(b). We note that β_1 and β_2 are negative for the parameter values we considered, because a net increase in sound speed produces a decrease in travel time and phase.

The calculation of β_3 is not as simple, because the $n = 3$ ray reflects above the SOFAR axis and the ray-family characterization useful for $n = 1$ and 2 does not apply. Level curves of β_3 were approximated from values of β_3 computed directly from Eqs. (18) and (19c). The computations were performed for values at the intersection points of a rectangular grid in the (α, R) plane. Each computation requires determination of the mean ray geometry, but the method is

straightforward. The results are shown in Fig. 7(c), along with the limiting curve 5 and directionality curve 6 from Fig. 3. The level curves have the same general shape as those in Figs. 7(a) and 7(b). As an example, to compute the value of β_3 for $(\alpha, R) = (10^\circ, 10 \text{ km})$, we note $d_R - d_O = 1.76$. The appropriate position is shown as a cross on Fig. 7(c). By linear interpolation, we find $\beta_3 = -1.07$.

We now develop a theoretical explanation for the behavior of total-field phase and amplitude for type I multipath behavior (and type II multipath between the entrance and exit times of a ray). We suppose $\bar{\Phi}$ and \bar{A} are the total-field phase and amplitude (relative to the unit-amplitude source) in the absence of sound-speed perturbations. We define $\Delta\Phi$ and $\Delta A/\bar{A}$ as the total-field phase and relative amplitude deviations due to perturbations, i.e.

$$\Delta\Phi \equiv \Phi(\hat{c}_A) - \Phi(c_A) = \Phi(t) - \bar{\Phi} \quad , \quad (20a)$$

and

$$\Delta A(t)/\bar{A} \equiv (A(\hat{c}_A) - A(c_A))/A(c_A) = (A(t) - \bar{A})/\bar{A} \quad . \quad (20b)$$

We note that $\Delta A/\bar{A}$ is the ratio of the amplitude deviation produced by the perturbations and the unperturbed amplitude. It follows from Eq. (20b) that the logarithmic amplitude anomaly is

$$\Delta L(t) \equiv 20 \log_{10}[1 + (\Delta A(t)/\bar{A})] = 20 \log_{10} A(t) - 20 \log_{10} \bar{A} \quad . \quad (20c)$$

Thus, knowledge of $\Delta A/\bar{A}$ determines, via Eq. (20c), the difference in decibels between the amplitudes with and without the perturbations. If $\Delta A/\bar{A}$ is sufficiently small, then ΔL is approximately equal to

(8.68) $(\Delta A/\bar{A})$.

We assume that variations in individual ray amplitudes from the perturbations have negligible effect on the total field. This assumption is confirmed numerically by results in Sec. III, and could be demonstrated analytically by the same methods used to confirm it in other problems (see, for example, Ref. 17). Thus, we regard each A_n as independent of time, and we need only consider the influence on $\Delta A/\bar{A}$ and $\Delta\phi$ of phase perturbations $\Delta\phi_n(t)$. We define, for $m \neq n$,

$$\epsilon_{mn}(t) \equiv \Delta\phi_m(t) - \Delta\phi_n(t), \quad 1 \leq m, n \leq 3, \quad (21a)$$

where ϵ_{mn} is the phase-perturbation difference, expressed in cycles, between rays m and n . We further assume that the maxima over t of any $2\pi\epsilon_{mn}(t)$, the perturbation differences expressed in radians, are sufficiently small compared to one. However, even values of $2\pi\epsilon_{mn}$ larger than 0.5 give acceptably-accurate approximations. Moreover, even though our formulas become particularly simple when the $2\pi\epsilon_{mn}$ are small, this assumption is not essential to our procedure. We also define $\delta\phi_n$ as the difference (in cycles) between the mean value of the phase of ray n and the mean total-field phase,

$$\delta\phi_n \equiv \phi_n(c_A) - \phi(c_A), \quad 1 \leq n \leq 3. \quad (21b)$$

Note that neither the $\Delta\phi_n$ nor the $\delta\phi_n$ are required to be small. The last assumption needed for our total-field approximation is that $\Delta A/\bar{A}$ be sufficiently small to expand the total-field equations in this quantity. Again, as with the parameter $2\pi\epsilon_{mn}$, even relatively large values of $\Delta A/\bar{A}$ near 0.5 give useful approximations.

Consider first the double-path cases. From Eqs. (17), (20), and (21), we find

$$(\bar{A} + \Delta A)^2 = A_m^2 + A_n^2 + 2A_m A_n \cos [2\pi(\delta\phi_m - \delta\phi_n + \epsilon_{mn})] , \quad (22a)$$

where m and n are the indices of the two rays involved. We expand Eq. (22a), neglecting terms involving $(\Delta A/\bar{A})^2$ and those with $(2\pi\epsilon_{mn})$ to powers higher than the first. Using Eqs. (17) to simplify the result, we obtain

$$\Delta A(t)/\bar{A} \doteq 2\pi\epsilon_{mn}(t)(A_n/\bar{A})\sin(2\pi\delta\phi_n), \quad (m \neq n) . \quad (22b)$$

An approximation for $\Delta L/(t)$ then follows from the first equality in Eq. (20c). Rewriting Eqs. (17) using Eqs. (20) and (21) leads to the formula

$$\begin{aligned} (\bar{A} + \Delta A)e^{2\pi i\Delta\phi} &= e^{2\pi i(\Delta\phi_m + \Delta\phi_n)/2} [A_m e^{i2\pi(\delta\phi_m + \epsilon_{mn}/2)} \\ &+ A_n e^{i2\pi(\delta\phi_n - \epsilon_{mn}/2)}] . \end{aligned} \quad (23a)$$

Expanding Eq. (23a) and simplifying with Eq. (22b) implies the approximation

$$\Delta\phi(t) \doteq \Delta\phi_m(t) - \epsilon_{mn}(t)(A_n/\bar{A})\cos(2\pi\delta\phi_n), \quad (m \neq n) . \quad (23b)$$

Thus, amplitude and phase changes of the total field are predicted to possess the same time behavior as $\hat{\Delta}(t)$, since each $\Delta\phi_m$, and hence each ϵ_{mn} , is proportional to $\hat{\Delta}(t)$.

We found very good agreement between predictions from Eqs. (22b) and (23b) and numerically-computed type I double-path results, described in Sec. III. The $(\alpha, R) = (11^\circ, 7 \text{ km})$ case, with $m = 1$ and

$n = 2$, is typical, and numerical calculations for $A(t)$ and $\phi(t)$ were discussed in connection with the solid curves on Fig. 4. The mean values are $A_1 = 1.72 \times 10^{-4}$, $A_2 = 1.31 \times 10^{-4}$, $\delta\phi_1 = 0.14$ cycles, $\delta\phi_2 = 0.75$ cycles, and $\bar{A} = 1.09 \times 10^{-4}$. As an example, at the minimum of $\hat{\Delta}$ (at $t = 9$ h), the values of $\Delta\phi_1$ and $\Delta\phi_2$ predicted from Eqs. (19a) and (19b) are -0.32 and -0.25 , respectively, and are virtually identical to the numerically-calculated values. With these numbers in Eq. (23b), we obtain $\Delta\phi(9) \doteq -0.32$ cycles, compared to the numerically-computed value of -0.31 cycles. Similarly, using Eqs. (22b) and (20c), we find that $\Delta L(9) \doteq 3.8$ dB, while the difference between the numerically-computed values of $20 \log_{10} A(9)$ and $20 \log_{10} \bar{A}$ is almost identical. Theoretical predictions for phase and amplitude are shown as dashed curves on Fig. 4; specifically, the amplitude curve is $20 \log_{10} \bar{A} + \Delta L(t)$ using Eqs. (20c) and (22b), while the phase curve is $\Delta\phi(t)$ from Eq. (23b) plus 1.0 cycles, to correspond to the way the solid curve was plotted. Wherever the theoretical curve is not shown, it is indistinguishable from the numerical results. As can be seen from Fig. 4, the maximum difference between the theoretical and numerical values occurs at the maximum of $\hat{\Delta}$ (i.e. $t = 3$ h), since the numerical results are slightly non-symmetric about $t = 6$ h. Nonetheless, the relative error in the theoretical predictions for amplitude, as an example, is less than 12% for all time, and typically the error is less than this. A similar comparison is shown for portions of the $(\alpha, R) = (12^\circ, 8 \text{ km})$ curves in Fig. 4. Even closer agreement is observed here.

For type I triple-path cases, formulas similar to Eqs. (22) and (23) may be developed. The analog to Eq. (22a) has six terms

on the right side, and with the same assumptions on $(\Delta A/\bar{A})^2$ and the $(2\pi\epsilon_{mn})^2$, it can be shown that

$$\dot{\Delta A} = 2\pi\epsilon_{23}(t) A_3 \sin(2\pi\delta\phi_3) + 2\pi\epsilon_{21}(t) A_1 \sin(2\pi\delta\phi_1). \quad (24a)$$

The analog to Eq. (23a) is expanded, assuming sufficiently small $(\Delta A/\bar{A})^2$ and $(2\pi)^2(\epsilon_{mn} + \epsilon_{mk})^2/9$, to obtain after simplification:

$$\begin{aligned} \Delta\phi = & \Delta\phi_2(t) - \epsilon_{21}(t)(A_1/\bar{A}) \cos(2\pi\delta\phi_1) \\ & - \epsilon_{23}(t)(A_3/\bar{A}) \cos(2\pi\delta\phi_3). \end{aligned} \quad (24b)$$

We note that in the manner they are written, Eqs. (24) represent direct extensions of Eqs. (22b) and (23b).

The approximations Eqs. (24) produce quite accurate predictions to the numerical results in every triple-path case we examined. Typical comparisons are shown in Fig. 6, with the same conventions as Fig. 4. In particular, for $(\alpha, R) = (8^\circ, 8 \text{ km})$, the mean values A_n are 1.49×10^{-4} , 1.01×10^{-4} , and 9.64×10^{-5} for $n = 1, 2, 3$; $\bar{A} = 1.66 \times 10^{-4}$; and $\delta\phi_n$ are 0.11, -0.02, and 0.67 cycles for $n = 1, 2, 3$. The theoretical values from Eqs. (19) for $\Delta\phi_n(3)$ are 0.42, 0.30, and 0.31 cycles for $n = 1, 2, 3$, compared to calculated values of 0.42, 0.30, and 0.32 cycles, respectively. The predictions from Eqs. (24) and (20c) for $\Delta\phi(3)$ and $20 \log_{10} \bar{A} + \Delta L(3)$ are 0.38 cycles and -80.1 dB, while the numerical values are 0.39 cycles and -81.0 dB. As before, agreement at other times is even closer. Also shown in Fig. 6 are comparisons for the type II case of $(\alpha, R) = (10^\circ, 10.5 \text{ km})$.

A particularly striking feature of these approximations is their success when the $2\pi\epsilon_{mn}$ are not particularly small with respect

to one. For the example just discussed, the maximum values of $2\pi\epsilon_{12}$ and $2\pi\epsilon_{13}$ are 0.76 and 0.67 radians. In fact, the derivation of our results suggests that they could be expected to produce good approximations so long as the $2\pi\epsilon_{mn}$ are merely less than one, rather than significantly smaller than one, with the important provision that $\Delta A/\bar{A}$ remain small. This condition is, of course, violated in type III multipath behavior and in type II cases at points when rays are lost or gained. We also remark that this type of approximation to the multipath field takes advantage of environmental variations producing small relative changes in the phases of individual ray arrivals, not on the specific assumptions of the environmental or acoustic model in this paper. Only the mean phase and amplitude of each ray, the mean total field, and expressions for the individual ray phase perturbations are required. The forms of Eqs. (24) suggest possible generalizations to problems in which the total field consists of more rays. Such approximations may prove useful in other problems where conditions for their validity are satisfied.

V. SUMMARY

In this paper we investigate the combined effects of sound-speed fluctuations and variable bottom depth on oceanic sound transmission. Off-shore propagation ranges are modeled by assuming a horizontal ocean surface, a uniformly-sloping bottom, a mean bilinear sound-speed structure, and bottomed source and receiver (above and below the SOFAR axis, respectively). In this

paper we consider propagation in the down-slope direction. Intervals of allowable values for the bottom-slope angle α and source-receiver distance R are considered. Sound-speed fluctuations are assumed to be due to the dominant upper-ocean temperature variations, as in a previous paper.¹ The model assumptions guarantee that rays consist of planar piecewise-circular arcs. For our particular assumptions, it is found that for each pair of integers $[K,L]$, there is at most one ray having K surface and L bottom reflections. However, the set of SRBR and RBR rays that does occur changes dramatically depending on parameter values. An example of some types of changes is given by Fig. 3, which shows regimes of existence of mean-state rays in the (α,R) plane, using fixed values of other parameters and a source-directionality condition. Based on this figure, subsequent investigations are restricted to parameter values for which the received total field has at most three contributing rays. It is emphasized that other model assumptions can easily enrich the possibilities for occurrence of rays, and the effects of factors such as different mean-state parameter values, different source and receiver positions, and piecewise-linear bottom models are discussed briefly.

With expressions for travel time, spreading loss, and boundary loss and phase shifts for the three rays, and including sound-speed fluctuations, the total field is computed numerically as a function of time. All single-path cases have amplitude virtually constant in time and show a simple proportionality

between received phase and sound-speed fluctuations. In contrast, three distinct patterns for the multipath cases are categorized, each of which may have significant amplitude variations. We denote by type I the majority of time evolutions observed, with roughly sinusoidal phase and amplitude curves, the latter showing peak-to-peak variations of up to about 10 dB. In type II behavior, the sound-speed fluctuations and sloping bottom conspire to produce the disappearance and later reappearance of a ray over a portion of the twelve-hour fluctuation period, leading to a jump in the amplitude and phase curves. This can occur for parameter values close to or on the curves in Fig. 3. A third type of amplitude and phase characteristics is possible, in which the time behavior differs sharply from that of the fluctuations. Type III behavior arises for special phase and amplitude relationships in the mean rays.

A theoretical explanation is developed for multipath behavior of type I and of the continuous portions of type II. Time variations of individual ray amplitudes can be shown to have negligible effect on total-field time dependence. Thus, the first step is to relate the phase variations of individual rays to the environmental fluctuations and the variables describing the mean ray geometry. Level curves of maximum phase perturbations are then constructed and discussed. The second step in the theory is to relate total-field variations to the ray-phase perturbations. Formulas for the deviations to the total-field phase and amplitude are derived. Then, predictions from the formulas are compared with numerical calculations. As

illustrated by Figs. 4 and 6, the comparisons show quite close agreement. The good accuracy of the theoretical formulas is discussed, in view of the conditions assumed for their derivation.

In future work the authors plan to extend the analysis to include other combinations of environmental effects and acoustic configurations, including depth-dependent currents and different source-receiver locations and ocean boundary models. For any such problems, characterizations similar to the two in this paper, of ray occurrence in terms of parameters and of types of total-field behavior, would be needed. Moreover, it is expected that the theoretical tool developed for approximating total-field variations would be useful.

REFERENCES

- ¹ K.G. Hamilton, W.L. Siegmann, and M.J. Jacobson, J. Acoust. Soc. Am. 62, 53-62 (1977).
- ² M.J. Jacobson and J.G. Clark, J. Acoust. Soc. Am. 41, 167-176 (1967).
- ³ M.J. Jacobson and J.T. Warfield, J. Acoust. Soc. Am. 43, 15-24 (1968).
- ⁴ J.T. Warfield and M.J. Jacobson, J. Acoust. Soc. Am. 52, 383-394 (1972).
- ⁵ R.N. Baer and M.J. Jacobson, J. Acoust. Soc. Am. 54, 80-91 (1973).
- ⁶ J.A. Widtfeldt and M.J. Jacobson, J. Acoust. Soc. Am. 59, 852-860 (1976).
- ⁷ R.N. Baer and M.J. Jacobson, J. Acoust. Soc. Am. 56, 809-816 (1974).
- ⁸ J.G. Clark, Institute for Acoustical Research, Miami, FL (private communication).
- ⁹ R. Hendry, Phil. Trans. Roy. Soc., London, A, 286, 1-24, (1977).
- ¹⁰ C. Wunsch and R. Hendry, Geophys. Fluid Dynamics 4, 101-145 (1972).
- ¹¹ M. Kronengold and W.J. Toulis, IEEE Trans. Geosci. Elect. 6, 204-211 (1968).
- ¹² K.V. Mackenzie, J. Acoust. Soc. Am. 32, 221-231 (1960).
- ¹³ N.L. Weinberg, J.G. Clark, and R.P. Flanagan, J. Acoust. Soc. Am. 56, 447-458 (1974).

- 14 R.N. Baer and M.J. Jacobson, J. Acoust. Soc. Am. 55, 1178-1189 (1974).
- 15 J.D. Kraus, Antennas (McGraw-Hill, New York, 1950), Secs. 4.4, 4.6a.
- 16 E.R. Franchi and M.J. Jacobson, J. Acoust. Soc. Am. 52, 316-331 (1972).
- 17 L.A. Stallworth and M.J. Jacobson, J. Acoust. Soc. Am. 48, 382-391 (1970).

FIGURE LEGENDS

- FIG. 1. Geometry of the propagation range and of three rays of principal interest.
- FIG. 2. Mean bilinear sound-speed profile and pivoting produced by fluctuations.
- FIG. 3. Existence regimes of various rays as functions of range R (km) and bottom-slope angle α (degrees). See text for explanation of numbered curves.
- FIG. 4. Relative total-field amplitude (dB) and phase (cycles) versus time (h) for mean double-path cases: $(\alpha, R) = (11^\circ, 7 \text{ km})$ and $(\alpha, R) = (12^\circ, 8 \text{ km})$. Solid curves computed numerically, dashed curves from theory in Sec. IV.
- FIG. 5. Relative total-field amplitude (dB) and phase (cycles) versus time (h) for $(\alpha, R) = (11^\circ, 15 \text{ km})$.
- FIG. 6. Relative total-field amplitude (dB) and phase (cycles) versus time (h) for mean triple-path cases: $(\alpha, R) = (8^\circ, 8 \text{ km})$ and $(\alpha, R) = (10^\circ, 10.5 \text{ km})$. Solid curves computed numerically, dashed curves from theory in Sec. IV.
- FIG. 7. Level curves of phase-perturbation coefficient of sound-speed deviation β_n (cycles $\text{m}^{-1} \text{ sec}$) in $(d_R - d_O, R)$ plane, for ray (a) $n=1$, (b) $n=2$, and (c) $n=3$. See text for explanation of numbered curves.

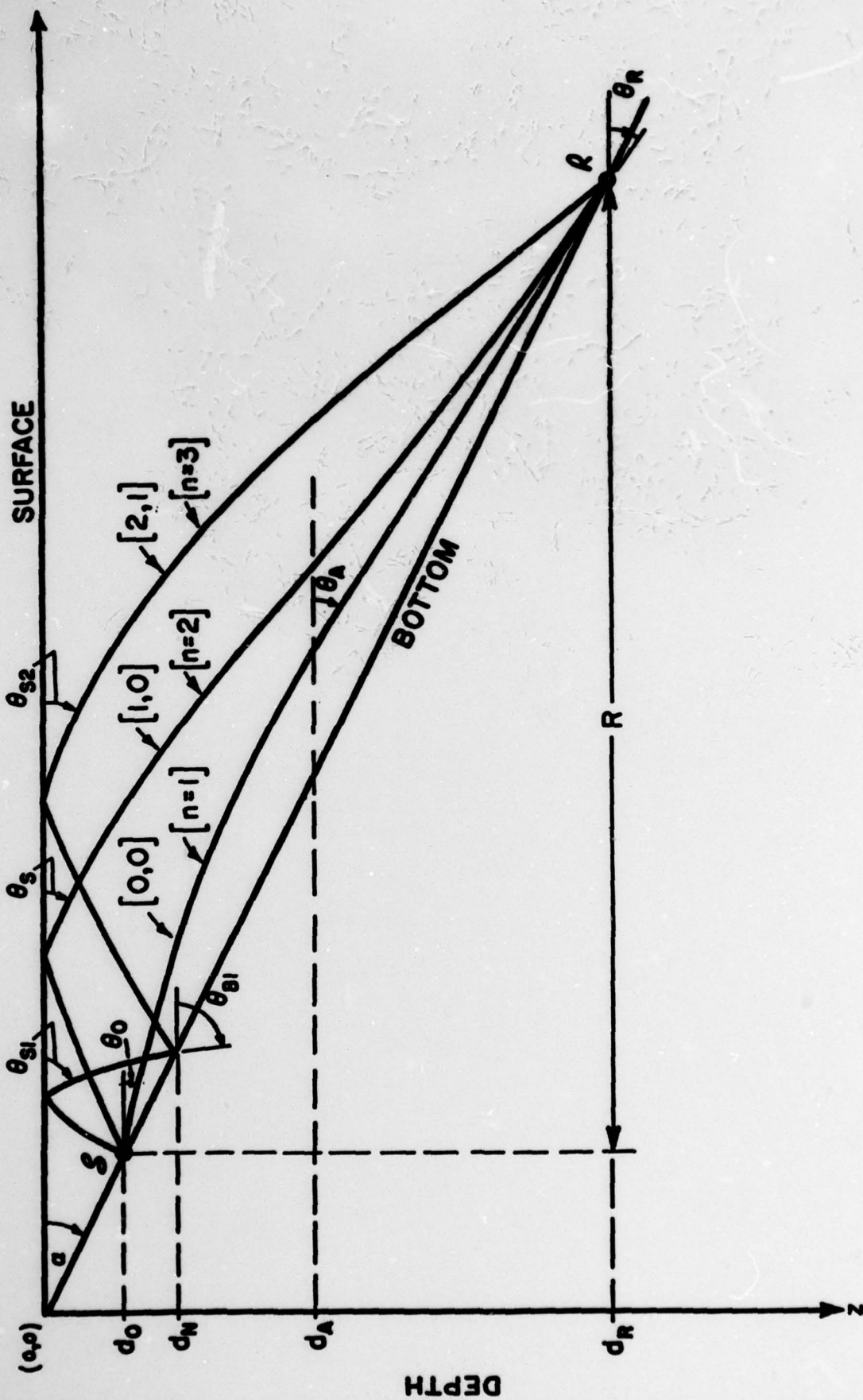


FIGURE 1

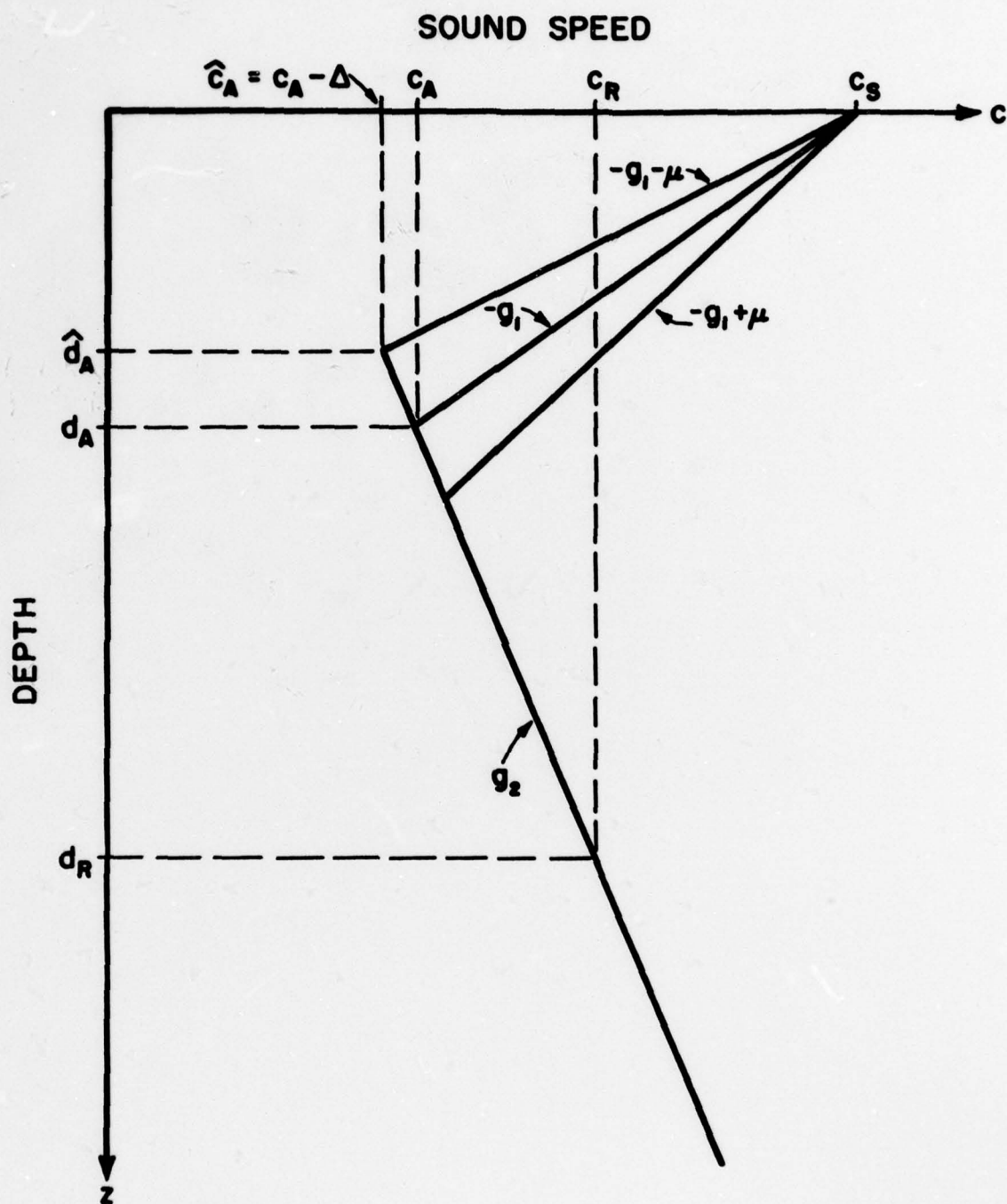


FIGURE 2

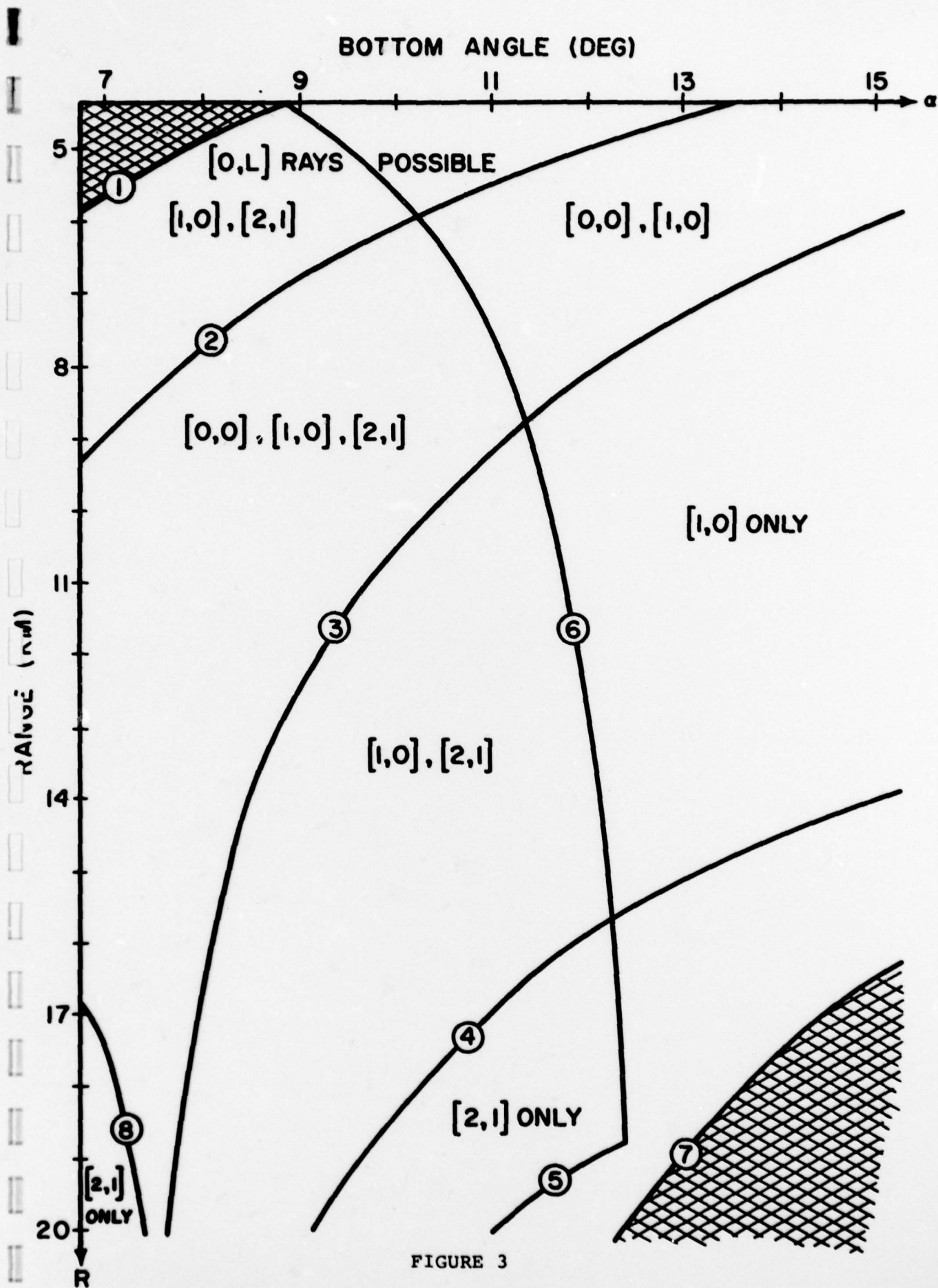


FIGURE 3

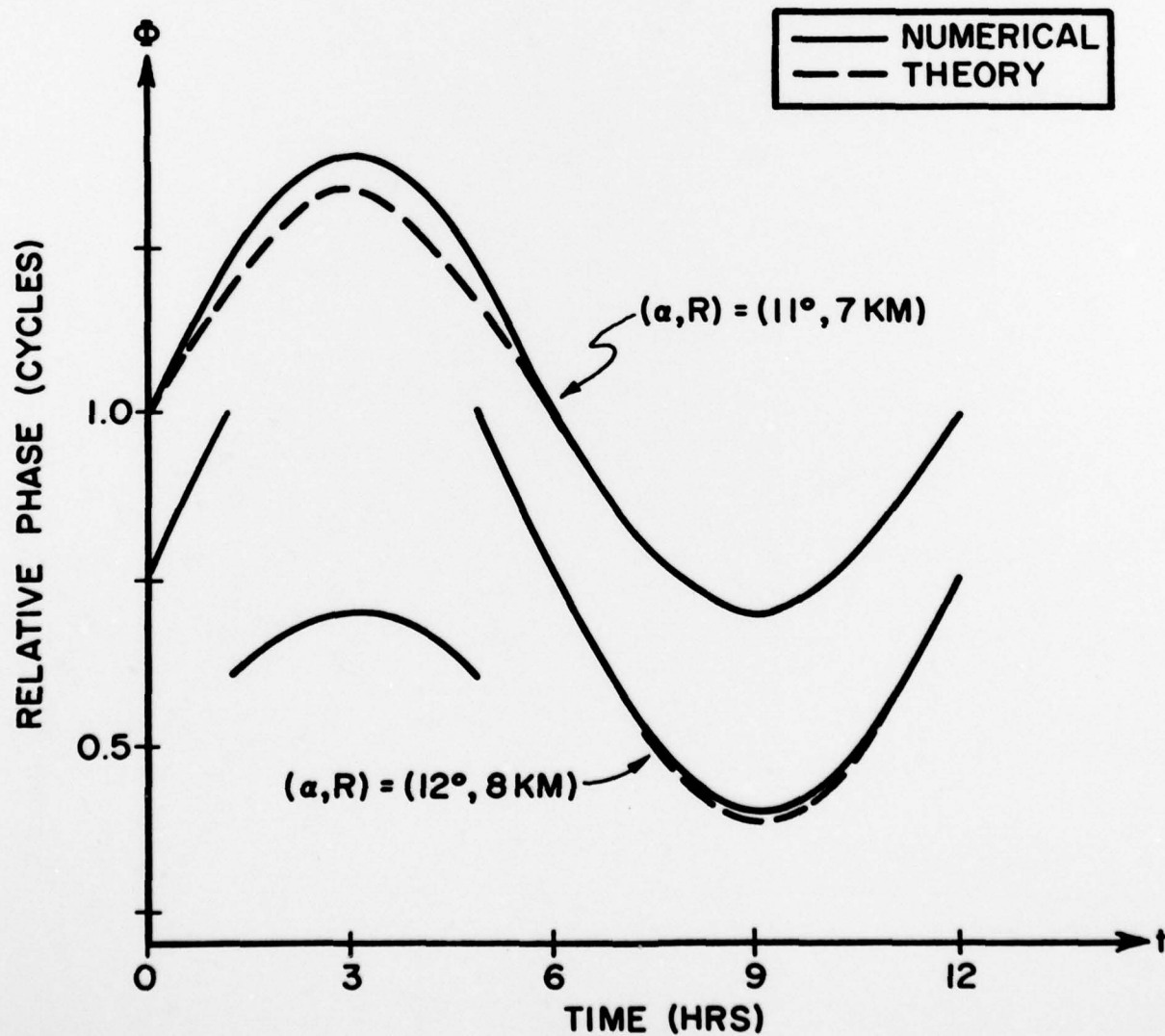
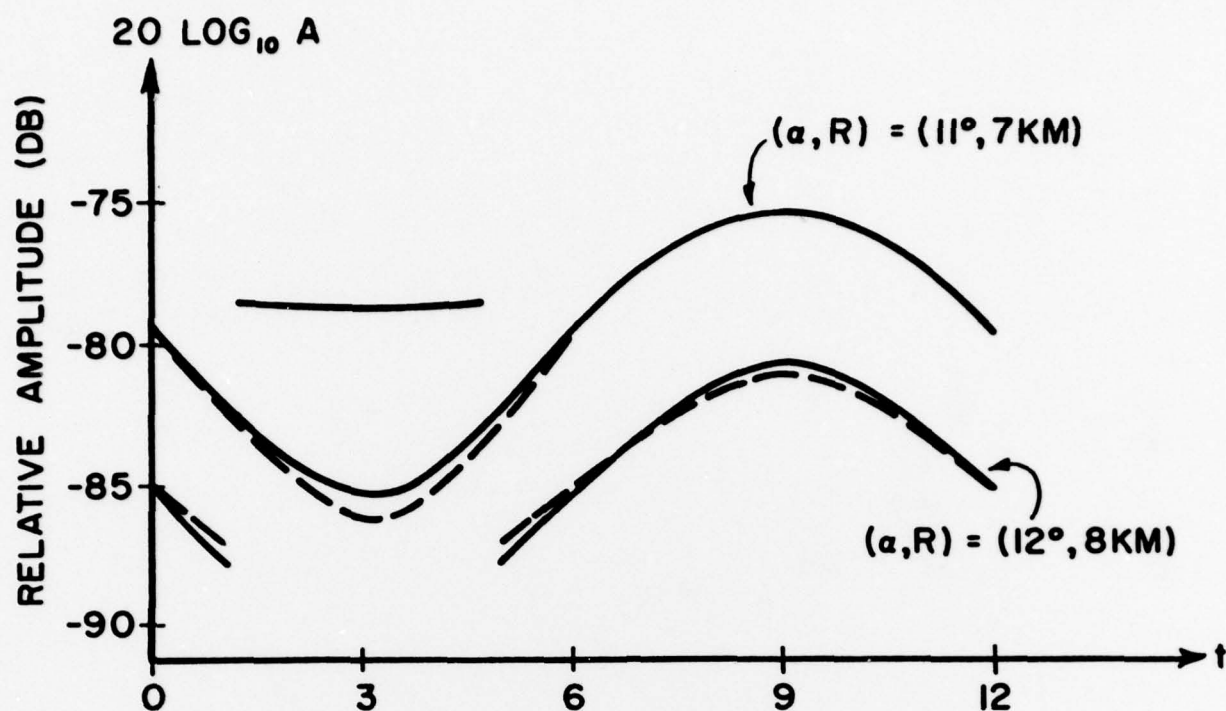


FIGURE 4

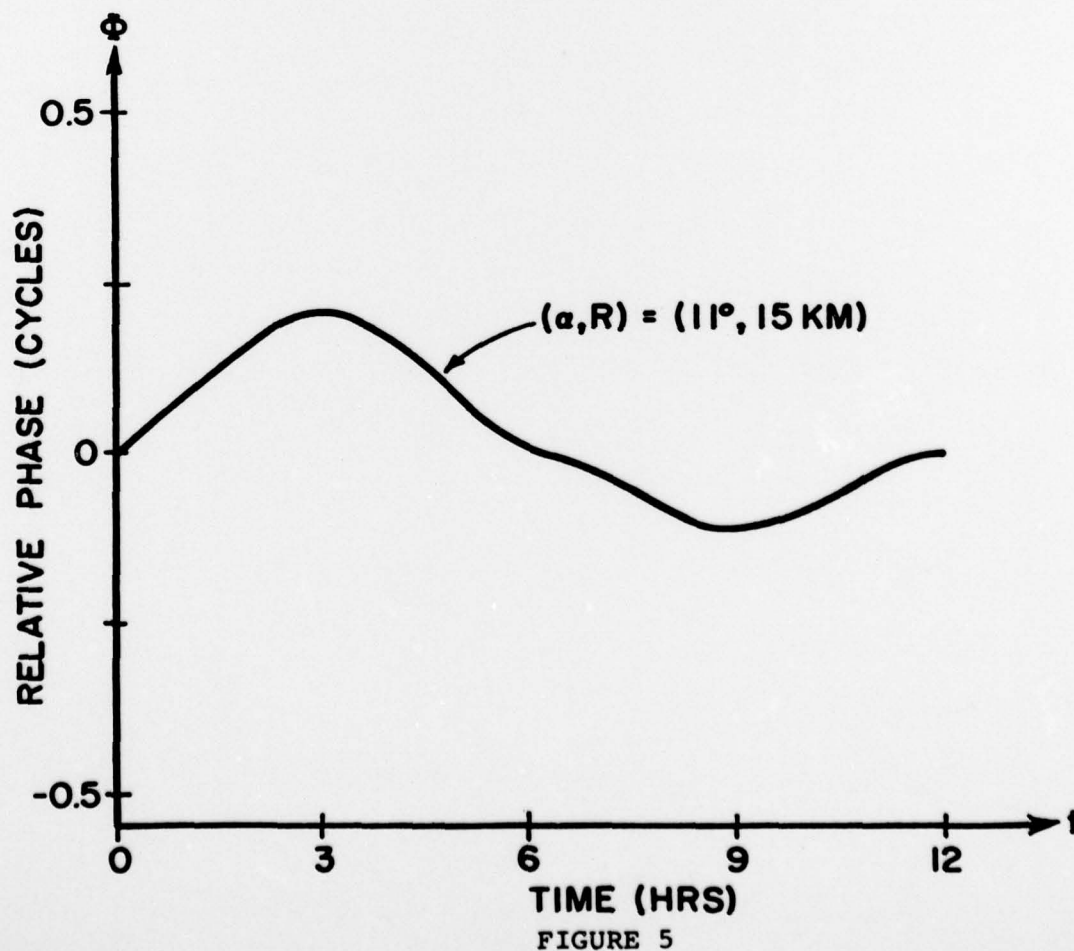
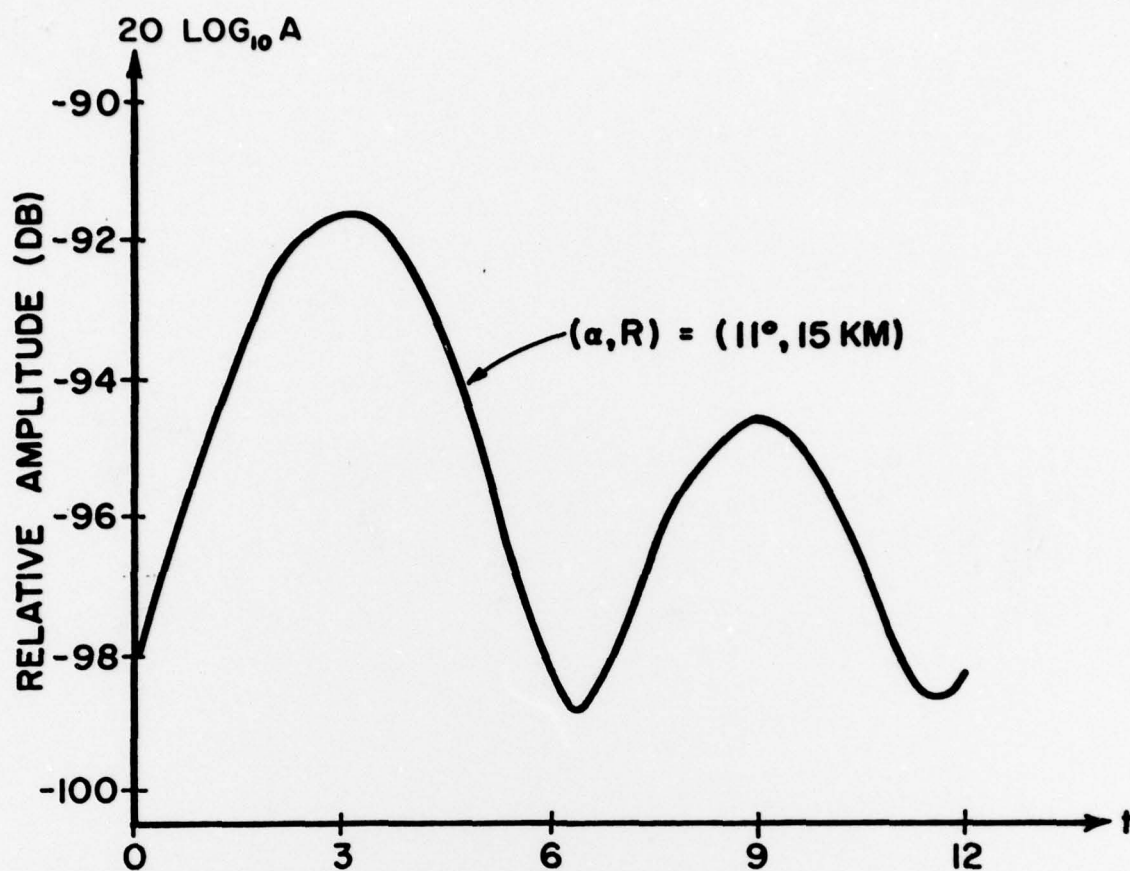


FIGURE 5

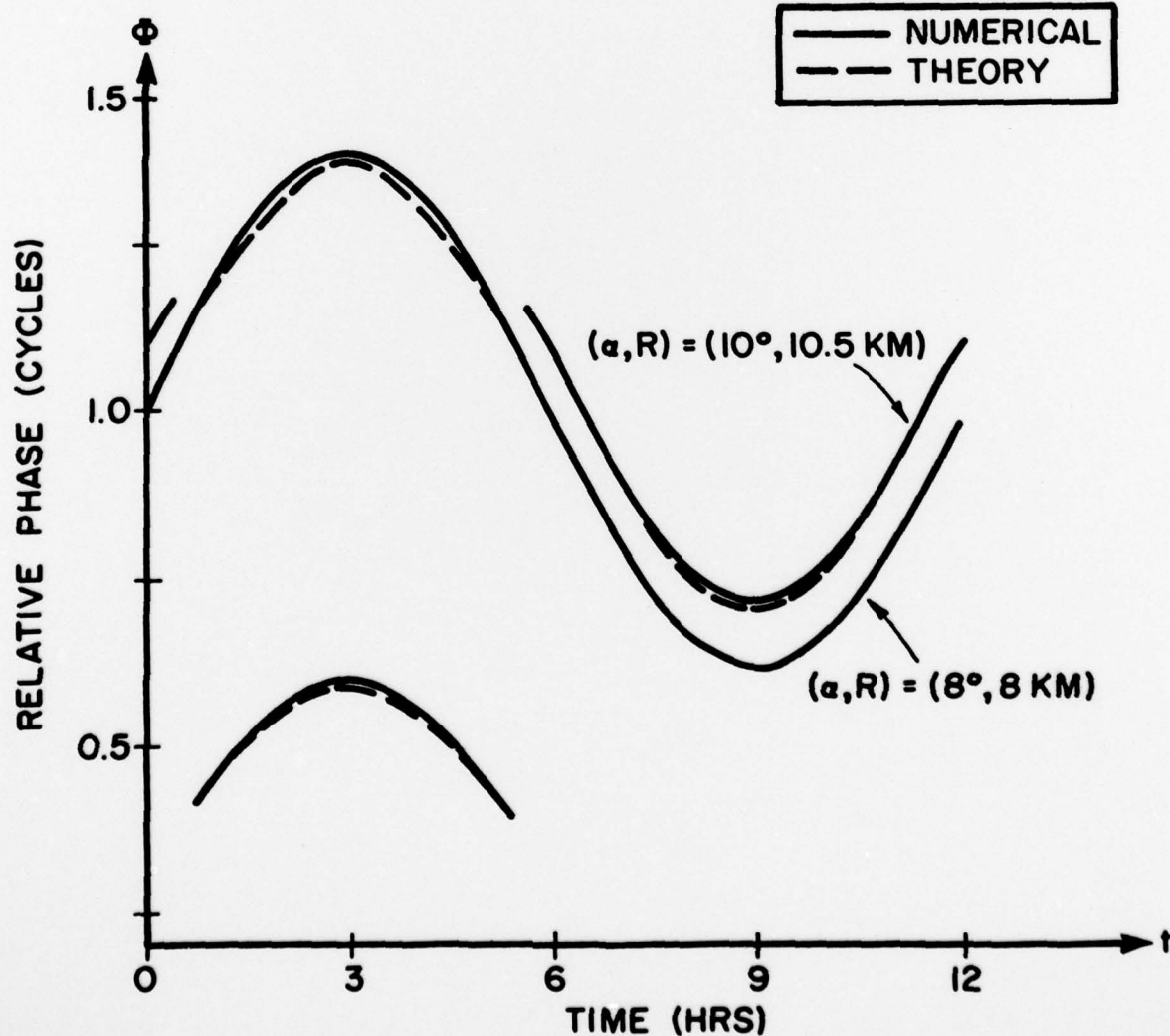
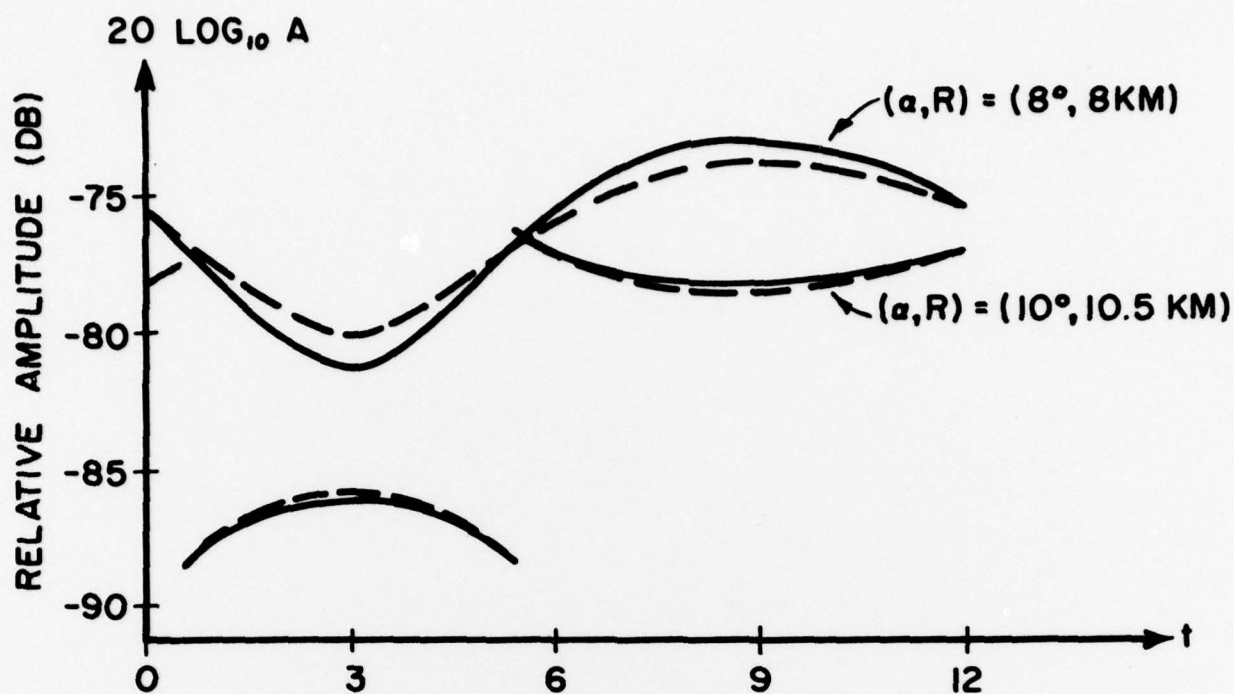


FIGURE 6

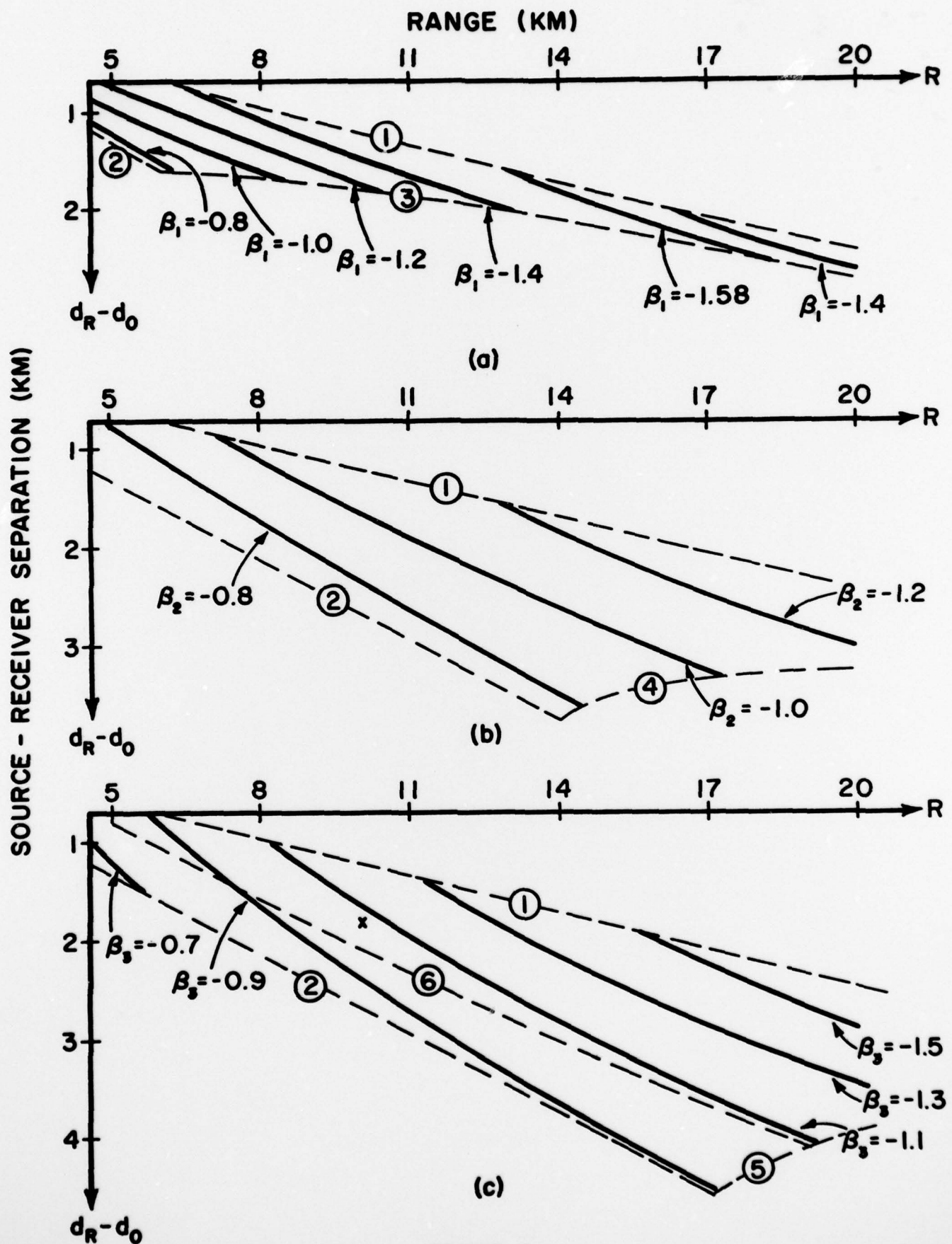


FIGURE 7

DISTRIBUTION LIST

Office of Naval Research (Code 222)	2
(Code 102-OS)	1
(Code 480)	1
Department of the Navy	
Arlington, Virginia 22217	
Director	6
Naval Research Laboratory	
Technical Information Division	
Washington, D. C. 20375	
Director	1
Office of Naval Research Branch Office	
1030 East Green Street	
Pasadena, California 91106	
Office of Naval Research	1
San Francisco Area Office	
760 Market Street - Room 447	
San Francisco, California 94102	
Director	1
Office of Naval Research Branch Office	
495 Summer Street	
Boston, Massachusetts 02210	
Office of Naval Research	1
New York Area Office	
207 West 24th Street	
New York, New York 10011	
Director	1
Office of Naval Research Branch Office	
536 South Clark Street	
Chicago, Illinois 60605	
Code 102 IP	(Uncl.) 8
Office of Naval Research	(No Class.
Arlington, Virginia 22217	Reports)
Commander	1
Naval Ordnance Laboratory	
Acoustics Division	
White Oak	
Silver Spring, Maryland 20910	
ATTN: Dr. Zaka Slawsky	

DISTRIBUTION LIST - 2

Officer in Charge 1
Annapolis Laboratory
Naval Ship Research and Development Center
Annapolis, Maryland 21402

Commander 1
Naval Sea Systems Command
Code SEA 037
Washington, D. C. 20362

Commander
Naval Sea Systems Command
Washington, D. C. 20362
ATTN: Mr. Carey D. Smith (Code SEA 06H1) 1
CDR Bruce Gilchrist (Code SEA 06H2) 1

Officer in Charge 1
Pasadena Laboratory
Naval Undersea Center
3202 East Foothill Boulevard
Pasadena, California 91107

Commanding Officer 1
Fleet Numerical Weather Central
Monterey, California 93940

Defense Documentation Center 20
Cameron Station
Alexandria, Virginia 22314

Chief of Naval Material 1
Department of the Navy
Washington, D. C. 20360
ATTN: Mr. James Probus (Acting Director
of Navy Laboratories)

Office of the Secretary of Defense 1
DD&E
Pentagon, Room 3E1040
Washington, D. C. 20350
ATTN: Mr. Allan D. Simon

Commander
Naval Electronic Systems Command
Washington, D. C. 20360
ATTN: CAPT J. Bajus (NAVELEX 03) 1
CDR A. Miller (NAVELEX 320) 1

DISTRIBUTION LIST - 3

Chief of Naval Operations Department of the Navy Pentagon, Room 5B718 Washington, D. C. 20350 ATTN: CAPT Robert B. Brunsted	1
Commander Naval Ship Research and Development Center Bethesda, Maryland 20034 ATTN: Mr. Craig Olson	1
Chief of Naval Operations Department of the Navy Pentagon, Room 4C559 Washington, D. C. 20350 ATTN: CDR A. H. Gilmore	1
Commander Naval Undersea Center San Diego, California 92132 ATTN: Dr. Dan Andrews Mr. Henry Aurand	1 1
Chief Scientist Navy Underwater Sound Reference Division P. O. Box 8337 Orlando, Florida 32806	1
Officer in Charge New London Laboratory Naval Underwater Systems Center New London, Connecticut 06320	1
Commander Naval Air Development Center Warminster, Pennsylvania 18974	1
Commander Naval Ship Research and Development Center Bethesda, Maryland 20034	1
Superintendent Naval Postgraduate School Monterey, California 93940	1
Commanding Officer Naval Coastal Systems Laboratory Panama City, Florida 32401	1
Commanding Officer Naval Underwater Systems Center Newport, Rhode Island 02840	1

DISTRIBUTION LIST - 4

Superintendent Naval Academy Annapolis, Maryland 21402	1
Commanding Officer Naval Intelligence Support Center 4301 Suitland Road Washington, D. C. 20390 ATTN: Dr. Johann Martinek Mr. E. Bissett	1 1
Commander Naval Sea Systems Command Code SEA 03E Washington, D. C. 20362	1
Dr. Melvin J. Jacobson Rensselaer Polytechnic Institute Troy, New York 12181	1
Dr. Charles Stutt General Electric Company P. O. Box 1088 Schenectady, New York 12301	1
Dr. Alan Winder MSB Systems, Inc. 110-16 72nd Avenue Forest Hills, New York 11375	1
Dr. T. G. Birdsall Cooley Electronics Laboratory University of Michigan Ann Arbor, Michigan 48105	1
Dr. Harry DeFerrari University of Miami Rosenstiel School of Marine and Atmospheric Sciences Miami, Florida 33149	1
Mr. Robert Cunningham Bendix Electronics Center 15825 Roxford Street Sylmar, California 91342	1
Dr. Stephen Wolff John Hopkins University Baltimore, Maryland 21218	1

DISTRIBUTION LIST - 5

Dr. M. A. Basin S. D. P., Inc. 15250 Ventura Boulevard, Suite 518 Sherman Oaks, California 91403	1
Commanding Officer New London Laboratory Naval Underwater Systems Center New London, Connecticut 06320 ATTN: Dr. Albert Nuttall	1
Dr. Walter Duing University of Miami Rosenstiel School of Marine and Atmospheric Sciences Miami, Florida 33149	1
Commanding Officer New London Laboratory Naval Underwater Systems Center New London, Connecticut 06320 ATTN: Dr. H. W. Marsh Dr. D. M. Viccione	1
Dr. David Middleton 127 East 91st Street New York, New York 10028	(Uncl.) 1
Dr. David Middleton c/o ONR New York Area Office 207 West 24th Street New York, New York 10011	(Class.) 1
Dr. Donald W. Tufts University of Rhode Island Kingston, Rhode Island 02881	1
Dr. Loren W. Nolte Department of Electrical Engineering FT-10 University of Washington Seattle, Washington 98195	1
Mr. S. W. Autrey Hughes Aircraft Company P. O. Box 3310 Fullerton, California 92634	1
Dr. Thomas W. Ellis Texas Instruments, Inc. 13500 North Central Expressway Dallas, Texas 75231	1

DISTRIBUTION LIST - 6

Mr. Robert Swarts
Applied Physics Laboratory
University of Washington
1013 Northeast Fortieth Street
Seattle, Washington 98195

1

Institute for Acoustical Research
Miami Division of the Palisades
Geophysical Institute
615 S. W. 2nd Avenue
Miami, Florida 33130
ATTN: Mr. M. Kronengold
Dr. J. Clark
Dr. C. Kimball

2

Mr. Carl Hartdegen
Palisades Geophysical Institute
Sofar Station
FPO New York 09560

1

Mr. Charles Loda
Institute for Defense Analyses
400 Army-Navy Drive
Arlington, Virginia 22202

1

Mr. Beaumont Buck
Polar Research Laboratory
123 Santa Barbara Avenue
Santa Barbara, California 93101

1

Dr. M. Weinstein
Underwater Systems, Inc.
8121 Georgia Avenue
Silver Spring, Maryland 20910

1

Dr. Thomas G. Kincaid
General Electric Company
P. O. Box 1088
Schenectady, New York 12301

1

Applied Research Laboratories
The University of Texas at Austin
P. O. Box 4029
Austin, Texas 78712
ATTN: Dr. Lloyd Hampton
Dr. Charles Wood
Dr. T. D. Plemons

4

Woods Hole Oceanographic Institute
Woods Hole, Massachusetts 02543
ATTN: Dr. Paul McElroy
Mr. R. Forter
Mr. R. Spindel

1

DISTRIBUTION LIST - 7

Dr. John Bouyoucos
Hydroacoustics, Inc.
321 Northland Avenue
P. O. Box 3818
Rochester, New York 14610

1

Systems Control, Inc.
260 Sheridan Avenue
Palo Alto, California 94306
ATTN: Mr. L. Seidman

1

Atlantic Oceanographic and Meteorological Laboratories
15 Rickenbacker Causeway
Miami, Florida 33149
ATTN: Dr. John Proni

1

Dr. C. N. K. Mooers
University of Miami
Rosenstiel School of Marine and
Atmospheric Sciences
10 Rickenbacker Causeway
Miami, Florida 33149

1

Unclassified

SECURITY CLASSIFICATION OF THIS PAGE (When Data Entered)

REPORT DOCUMENTATION PAGE		READ INSTRUCTIONS BEFORE COMPLETING FORM
1. REPORT NUMBER RPI Math. Rep. No. 123	2. GOVT ACCESSION NO.	3. RECIPIENT'S CATALOG NUMBER
4. TITLE (and Subtitle) EFFECTS OF TIDALLY-VARYING SOUND SPEED ON ACOUSTIC PROPAGATION OVER A SLOPING OCEAN BOTTOM		5. TYPE OF REPORT & PERIOD COVERED Technical Report
7. AUTHOR(s) W.L. Siegmann, M.J. Jacobson, K.G. Hamilton		6. PERFORMING ORG. REPORT NUMBER
8. PERFORMING ORGANIZATION NAME AND ADDRESS Rensselaer Polytechnic Institute Troy, New York 12181		9. CONTRACT OR GRANT NUMBER(s) N 00014-76-C-0288
11. CONTROLLING OFFICE NAME AND ADDRESS Office of Naval Research, Code 222 Department of the Navy Arlington, Virginia 22217		10. PROGRAM ELEMENT, PROJECT, TASK AREA & WORK UNIT NUMBERS NR 386-606
14. MONITORING AGENCY NAME & ADDRESS (if different from Controlling Office)		12. REPORT DATE 1 February 1979
		13. NUMBER OF PAGES 52
		15. SECURITY CLASS. (of this report)
		15a. DECLASSIFICATION/DOWNGRADING SCHEDULE
16. DISTRIBUTION STATEMENT (of this Report) This document has been approved for public release and sale; its distribution is unlimited.		
17. DISTRIBUTION STATEMENT (of the abstract entered in Block 20, if different from Report)		
18. SUPPLEMENTARY NOTES		
19. KEY WORDS (Continue on reverse side if necessary and identify by block number) Bottom Effects Tides Acoustical Fluctuations		
20. ABSTRACT (Continue on reverse side if necessary and identify by block number) The influence of sound-speed fluctuations on propagation of a CW signal in an ocean with a uniformly-sloping bottom and a horizontal surface is analyzed using ray theory. The mean sound- speed structure is modeled as bilinear, with bottomed source and receiver above and below the SOFAR axis, respectively. The horizontally-independent fluctuations oscillate with a 12-h (over please)		

DD FORM 1 JAN 73 1473

EDITION OF 1 NOV 65 IS OBSOLETE
S/N 0102-LF-014-6601

Unclassified

SECURITY CLASSIFICATION OF THIS PAGE (When Data Entered)

Unclassified

SECURITY CLASSIFICATION OF THIS PAGE (When Data Entered)

period in the upper ocean. An examination is made of possible types of rays for down-slope propagation that might exist, depending on bottom-slope angle and source-receiver separation. The total acoustic field is investigated for its dependence on these parameters and time. For certain conditions when up to three rays comprise the mean total field, three patterns of time evolution are described, each of which may have significant amplitude variations. Numerically-computed examples of each type are presented. The linear relationships between phase variations of individual rays and the sound-speed fluctuations are derived. Then, formulas are developed to explain the most frequent behavior of the relative amplitude and phase of the multipath total field. Predictions from the formulas show very good agreement with the numerical calculations.

Unclassified

SECURITY CLASSIFICATION OF THIS PAGE (When Data Entered)